1

Numerical methods for molecular and continuum dynamics

Tony Ladd

Department of Chemical Engineering
University of Florida
Gainesville, Florida 32611-6005
tladd@che.ufl.edu

Abstract

In these lectures I will describe numerical techniques for integrating equations of motion that commonly occur in molecular and mesoscale simulations. We will begin by considering some simple examples of the overdamped "Brownian" limit, with and without hydrodynamic interactions. Comparisons of inertial (Langevin) simulations with conventional Brownian dynamics methods will be made for some simple test problems. Then I will outline the ideas behind symplectic integration of Hamiltonian systems and describe how numerical methods can be derived by the technique of "Operator Splitting". These ideas can be extended to Langevin dynamics by including dissipation and noise. Moving to Hamiltonian partial differential equations, we encounter an additional difficulty that the spatial discretization must preserve the canonical structure as well. In general, finite-difference and finite-element approximations do not have this property, and the long-time integration of wave equations, for example, is notoriously difficult. I will take a flexible elastic rod as an illustrative problem and show how a fully symplectic algorithm can be constructed. I will use numerical examples of explicit and implicit symplectic integrators, which suggest that operator splitting is the most computationally efficient approach. Finally we will consider the addition of thermal fluctuations to these systems.

1.1 Introduction

In these lectures we will be concerned with numerical integration of the Langevin equation,

$$m\dot{q} = p,\ \dot{p} = F - \gamma p + R(t). \tag{1.1}$$

The force F and friction $\xi = m\gamma$ are functions of q only (not p) and R is a random force with the usual statistical properties,

$$\langle R(t)\rangle = 0,\ \langle R(t)R(t')\rangle = 2\xi T\delta(t-t'). \tag{1.2}$$

The Langevin equation describes particles in a conservative force field F, but which are thermalized by a large number of fast degrees of freedom, for example a solvent. The key idea is to break down the forces exerted by the solvent into a systematic (drag) force, characterized by the friction coefficient ξ and a random force R; the fluctuation-dissipation theorem demands the relation between R and F given in Eq. 1.2 as a condition for thermal equilibrium at the temperature T.

The Langevin equation is widely applicable as a prototype description of coarse-grained molecular systems; of course it reduces to conservative molecular dynamics in the limit $\xi \to 0$. It also describes the dissipative dynamics of macroscopic particles in the limit that $T \to 0$ (no Brownian motion). We can parametrize q, p on a discrete set of integers, $[q_i, p_i]$, to describe a system of interacting particles, or on coordinates, $[q(s), p(s)]$, to describe continuous media. Here we will only consider a one-dimensional parametrization, which describes an elastic filament or rod. Two-dimensional parametrizations describe surfaces, for example membranes, vesicles and cells, but are much more complicated geometrically.

Standard numerical methods for ordinary and partial differential equations do not make use of any special structure or properties of the exact solutions. However, for Hamiltonian systems, there is a class of integrators that preserve the canonical structure of the exact equations of motion; these are called "symplectic" integrators. The Verlet leapfrog algorithm is an example of a symplectic integrator derived from "Operator Splitting", and provides a more accurate solution of the long-time dynamics than higher order but non-symplectic methods, such as explicit Runga-Kutta or predictor-corrector algorithms. The earliest symplectic integrators were based on implicit Runga-Kutta methods, but these require multiple force evaluations and are typically less efficient than operator splitting, which is fully explicit. The application of symplectic integrators is now well established in the molecular simulation community, but what is less well known is that these ideas can be applied to certain classes of partial differential equations as well; for example those pertaining to elasticity, fluid dynamics, and relativity. Applications of symplectic methods to continuum systems are limited and relatively recent; they may provide fruitful ground for further research.

The focus will be on numerical methods to integrate the equations of motion of these systems and the lectures are structured around specific examples more than general theory. I have worked out a number of simple problems to illustrate the key ideas and example programs can be found at http://ladd.che.ufl.edu/kmz09.tgz. The GNU scientific library is needed for the random number generators (http://www.gnu.org/software/gsl). The interested reader is invited to write their own programs to solve some of the examples.

1.2 Example 1: Brownian oscillator

A single particle with constant friction in a linear force field has the equation of motion

$$\dot{p} = -kq - \gamma p + R(t). \tag{1.3}$$

This is a linear Langevin equation and can be solved exactly [25]. To begin with we will consider a strongly overdamped oscillator, $\gamma \gg \sqrt{k/m}$. In this case we can drop the inertial term ($\dot{p}$), and the momentum equation is then just a force balance; substituting into the equation for $\dot{q}$, we obtain a stochastic differential equation for the coordinate,

$$\dot{q} = -\Omega q + r(t), \tag{1.4}$$

where $\Omega = k/\xi$, and the random velocity r has the covariance matrix

$$\langle r(t)r(t')\rangle = 2\xi^{-1}T\delta(t-t'). \tag{1.5}$$

Actually, this derivation is not entirely correct, as we shall see in Sec. 1.6, but it is sufficient when the random force is independent of q. Equation (1.4) is a specific instance of a more general class of stochastic differential equations comprising a drift velocity $v = \xi^{-1}F$ and a diffusive term; in the molecular simulation community this is frequently referred to as "Brownian dynamics". Equation (1.4) has the formal solution for a given initial displacement q_0,

$$q(t) = q_0 e^{-\Omega t} + e^{-\Omega t}\int_0^t e^{\Omega t'} r(t')dt', \tag{1.6}$$

with a time-dependent second moment,

$$\left\langle q^2(t)\right\rangle = q_0^2 e^{-2\Omega t} + \frac{T}{\kappa}\left(1 - e^{-2\Omega t}\right), \tag{1.7}$$

which can be used to check numerical simulations.

In the literature of stochastic differential equations (SDE's), for example the excellent book by Kloeden and Platen [14], the SDE is written in incremental form,

$$dq_t = -\Omega q_t dt + \sqrt{2D}\, dW_t, \tag{1.8}$$

where $D = T/\xi$, and the notation X_t is used to denote the value of the stochastic process X at time t. The term dW_t is an increment of a Wiener process W_t, which is a piecewise continuous function that is most simply described as a succession of random increments, $W_{t_1}, W_{t_2}, W_{t_3}, \ldots$. Each increment $dW_{t_i} = W_{t_{i+1}} - W_{t_i}$ is sampled from a normal distribution with zero mean and variance $t_{i+1} - t_i$. The properties of a Wiener process can be summarized in the following relations:

$$W_0 = 0,\ \langle W_t\rangle = 0,\ \left\langle (W_t - W_s)^2\right\rangle = |t-s| \tag{1.9}$$

Stochastic integrals with respect to W_t, can be defined as limits of Riemann sums in much the same way as integrals of analytic functions,

$$I_t = \int_0^t X_{t'} dW_{t'} = \lim_{n\to\infty} \sum_{i=1}^{n} X_{t_{i-1}} \left(W_{t_i} - W_{t_{i-1}} \right), \tag{1.10}$$

but with a number of subtle mathematical considerations, which we will systematically ignore.

Exercise 1. Given $X(t) = e^{\Omega t}$ in Eq. (1.10)*, use the properties of the Wiener process to show that the expectation values $\langle I_t \rangle = 0$ and $\left\langle I_t^2 \right\rangle = (2\Omega)^{-1} \left(e^{2\Omega t} - 1 \right)$.*

A simple approximate integration scheme, known as Euler or Euler-Maruyama, follows immediately from Eq. (1.8)

$$q_{t+\Delta t} = q_t - \Omega q_t \Delta t + \sqrt{2D\Delta t}\, \phi_t, \tag{1.11}$$

where ϕ_t is a Gaussian random variable (GRV) with zero mean and unit variance. Given an algorithm to generate random numbers with a Gaussian distribution (for instance from the GSL library), we can write a simple program to find q_n at a sequence of time intervals $t_n = n\Delta t$,

$$q_{n+1} = q_n \left(1 - \Omega\Delta t\right) + \sqrt{2D\Delta t}\, \phi_n. \tag{1.12}$$

The solution at time t_n,

$$q_n = q_0(1 - \Omega\Delta t)^n + \sqrt{2D\Delta t} \sum_{i=0}^{n-1} (1 - \Omega\Delta t)^{n-i-1} \phi_i \tag{1.13}$$

deviates from the exact solution of the same Wiener process,

$$q_{t_n} = q_0 e^{-\Omega t_n} + \sqrt{D\left(\frac{1 - \exp^{-2\Omega\Delta t}}{\Omega}\right)} \sum_{i=0}^{n-1} e^{-\Omega t_{n-i-1}} \phi_i \tag{1.14}$$

by terms proportional to Δt.

A more interesting example includes a q dependence in the diffusion coefficient; the linear SDE,

$$dq = -\Omega q dt + \sqrt{2D}\, q dW_t, \tag{1.15}$$

is driven by "multiplicative noise", as opposed to "additive noise" in Eq. (1.8). Multiplicative noise, meaning that the diffusion coefficient depends on q, adds greatly to the complexity of both theoretical analysis and numerical solutions of SDE's. Brownian dynamics simulations including hydrodynamic interactions are a common example of SDE's with multiplicative noise. We will return to this topic in Sec. 1.4.

Equation (1.15) is analytically soluble [14],

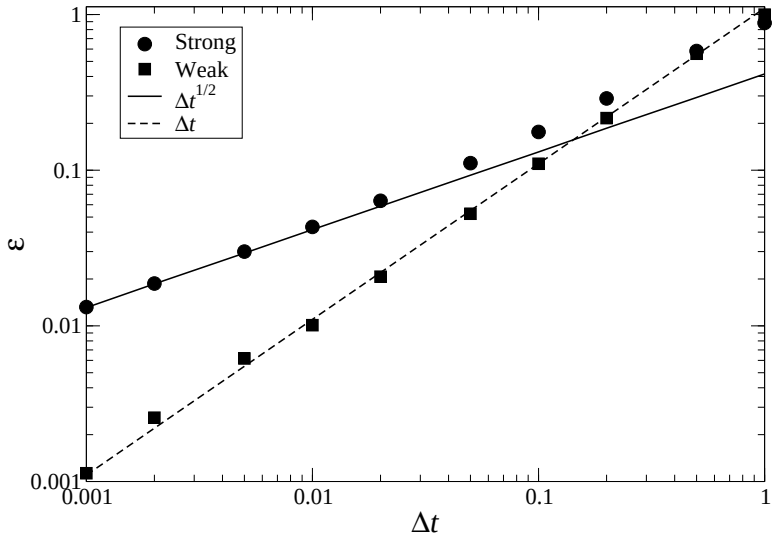

Fig. 1.1. Strong and weak convergence of the Euler method for a Brownian oscillator. The parameters Ω and D in Eq. (1.8) were set to unity and the trajectories were sampled after a time of 1. The average deviation in the trajectories was determined as a function of time step, Δt, from an ensemble of 10^8 initial conditions.

$$q_{t_n} = q_0 \exp\left[-(\Omega + D)t_n + \sqrt{2D\Delta t}\sum_{i=0}^{n-1}\phi_n\right], \tag{1.16}$$

and we can compare the exact and approximate solutions for the same Wiener process, defined at the time intervals $n\Delta t$. This is known as "strong convergence" and is formally defined in terms of the expectation value of the coordinate at a time t,

$$\epsilon(\Delta t) = \langle |q_{t_n} - q_n| \rangle \,. \tag{1.17}$$

The data in Fig. 1.1 shows that the Euler method for SDE's with multiplicative noise converges as the square root of time step, $\epsilon(\Delta t) \propto \Delta t^{1/2}$, whereas for deterministic differential equations it converges linearly in the time step. This introduces a pervasive problem with numerical solutions of SDE's, namely the difficulty of developing algorithms with a reasonable degree of convergence. We will return to this point later.

Strong convergence assures a controlled approximation to a given stochastic process or trajectory. Frequently, we are interested in average properties, for example the second moment $\langle q^2 \rangle$, or more generally some polynomial of q, $\langle P(q) \rangle$. Weak convergence of order β is defined in terms of the error in expectation values,

$$\epsilon(\Delta t) = \langle P(q_{t_n}) \rangle - \langle P(q_n) \rangle \propto \Delta t^{\beta}. \tag{1.18}$$

In Fig. 1.1 we see that the Euler algorithm has weak first order convergence for the SDE defined in Eq. (1.15), and in fact this is generally true. Numerical methods for weak approximations are easier, since the Wiener integrals can be replaced by simpler functions, $\hat{W}_t$, that match a specific number of moment conditions:

$$\left\langle \hat{W}_{t_n} \right\rangle = 0, \tag{1.19}$$

$$\left\langle \hat{W}^2_{t_n} \right\rangle = \Delta t, \tag{1.20}$$

$$\left\langle \hat{W}^3_{t_n} \right\rangle = 0, \tag{1.21}$$

$$\left\langle \hat{W}^4_{t_n} \right\rangle = 3\Delta t^2. \tag{1.22}$$

A first-order algorithm needs only the first two moments, while a second-order method needs the first four [14].

Exercise 2. Using the analytic solution in Eq. (1.16)*, show that the Euler algorithm converges strongly as* $\Delta t^{1/2}$*. Then show that weak convergence is order* Δt*.*

1.3 Example 2: FENE oscillator

The FENE (finitely extensible nonlinear elastic) potential is commonly used to represent a flexible polymer [21]. The force is linear at small extensions, but imposes a limit on the overall extension of the spring, corresponding to the contour length of the chain, q_{max},

$$F(q) = -\frac{\kappa q}{1 - q^2/q^2_{max}}. \tag{1.23}$$

The FENE interaction introduces a stiff non-linear force when the polymer is near its maximum extension and this requires a smaller time step than a purely linear force; the Euler algorithm leads to overextended bonds if the time step is larger than 0.1 (for $\kappa = D = 1$). The 2nd and 4th cumulants are readily calculated,

$$\langle q^2 \rangle = \frac{T}{\kappa}\left(\frac{\kappa q^2/T}{\kappa q^2/T + 3}\right), \tag{1.24}$$

$$\langle q^4 \rangle = \frac{T}{\kappa}\left(\frac{3(\kappa q^2/T)^2}{(\kappa q^2/T + 3)(\kappa q^2/T + 5)}\right), \tag{1.25}$$

and can be used to test the convergence of the numerical method. Once again we find weak linear convergence with time step, as shown in Fig. 1.2.

Exercise 3. Derive the results in Eqs. (1.24)–(1.25)*.*

For non-linear forces, the use of Gaussian random numbers is problematic, since very large displacements are occasionally generated. Unphysical

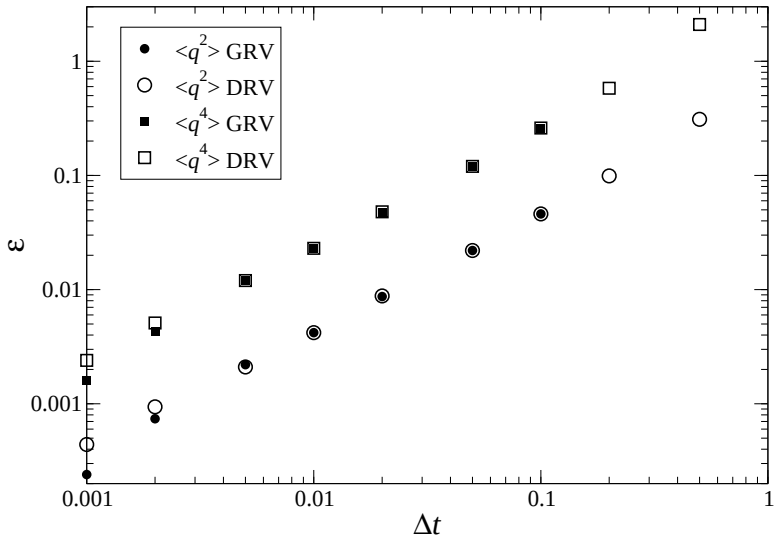

Fig. 1.2. Convergence of the cumulants $\langle q^2 \rangle$ and $\langle q^4 \rangle$ for a FENE spring. Numerical results from 10^6 trajectories are compared with the analytic solutions, Eqs. (1.24) and (1.25). Each trajectory was sampled for a time of 100 after an equilibration time of 10. The parameters $\kappa = D = 1$ and $q_{max} = 5$. The errors in the cumulants obtained with Gaussian random variables (solid symbols) and discrete random variables sampled from Eq. (1.27) (open symbols) are compared.

configurations can occur, in which the distance between the beads is larger than q_{max}, which limits the time step to smaller values than for a purely linear force. Since most statistical physics problems involve ensemble average properties, we can make use of the weak convergence property and substitute bounded distributions of random numbers for the Gaussian random variables used up to now. The simplest bounded random variable is a uniform distribution on the interval $[-1, 1]$, which satisfies the first three moment conditions, Eqs.(1.19)–(1.21) and is suitable for algorithms with convergence up to $\Delta t^{3/2}$. More typically we use discrete random variables (DRV's), which can be constructed to satisfy any number of moment conditions; for example the discrete distribution [14]

$$P(x) = \frac{1}{6}\delta(x + \sqrt{3}) + \frac{2}{3}\delta(x) + \frac{1}{6}\delta(x - \sqrt{3}) \tag{1.26}$$

has only six states yet matches the moment conditions up to 5th order. DRV's are also much faster to calculate than GRV's. A further refinement is to generate more than one DRV from a single 32-bit random number. For example, the distribution

$$P(x) = \frac{1}{8}\delta(x + a_+) + \frac{1}{8}\delta(x + a_-) + \frac{1}{2}\delta(x) + \frac{1}{8}\delta(x - a_-) + \frac{1}{8}\delta(x - a_+), \tag{1.27}$$

with $a_\pm = (2\pm\sqrt{2})^{1/2}$, has 8 states and so we can generate 10 random numbers from a single 32-bit word. This is preferable to the 6-state distribution in Eq. (1.26) which does not match exactly to a fixed number of bits. Further details can be found in the short paper included with the supplementary materials. The results using the 8-state DRV, Eq. (1.27) are identical to those obtained with GRV's within statistical errors (Fig 1.2).

1.4 Example 3: Hydrodynamic interactions

Hydrodynamic interactions are forces between suspended particles that are transmitted by fluid motion. A moving particle sets the fluid around it in motion, which influences the dynamics of even distant particles. At small Reynolds numbers, the hydrodynamic interactions can be approximated as a dissipative force, balanced by correlated fluctuating forces. Let us consider the simple example of a small Brownian particle, pushed towards a planar boundary by, for example, an optical trap. The equation of motion is again a Langevin equation, as in Eq. (1.3), but with a position dependent friction coefficient, $\xi(q) = 6\pi\eta a^2/q$, where a is the radius of the sphere and q is the minimum distance of the particle surface from the wall. This result can be derived from lubrication theory and becomes exact (in the Stokes-flow limit) as the particle gets close to the wall.

In the Brownian (inertialess) limit we obtain the following SDE for the particle coordinate,

$$dq = \xi_0^{-1} qF(q)\Delta t + \sqrt{2D_0 q}\, dW_t, \tag{1.28}$$

where $D_0 = T/\xi_0$ is the diffusion coefficient of the sphere far from the wall and q has been made dimensionless by the sphere radius a. We take a simple form for the force, $F = q^{-1} - q$, representing a repulsive force from the wall and a linear force from the trap. The even cumulants of q have the general form $\langle q^{2n}\rangle = (1+T)(1+3T)\ldots(1+(2n-1)T)$, where T is the non-dimensional temperature. The calculation is similar to the one in Exercise 3. We use the first two even cumulants,

$$\langle q^2\rangle = 1 + T,\ \langle q^4\rangle = 1 + 4T + 3T^2, \tag{1.29}$$

to check the convergence of the Euler method. Since we found problems with particles crossing the wall when $T = 1$ we take $T = 0.5$ in the following tests.

Exercise 4. By considering the Euler algorithm, without HI, explain why there is an upper bound to T in order to prevent wall crossings. Show that in the limit $\Delta t \to 0$, there can be no crossings if $T < 2/\phi_{max}^2$, where ϕ_{max} is the maximum value of the random variable ϕ. Note that with Gaussian random variables, we would not be able to prevent wall crossings. Explain why, when $T = 0.5$, there are no crossings if $\Delta t = 0.146$, but there are crossings if $\Delta t = 0.1465$.

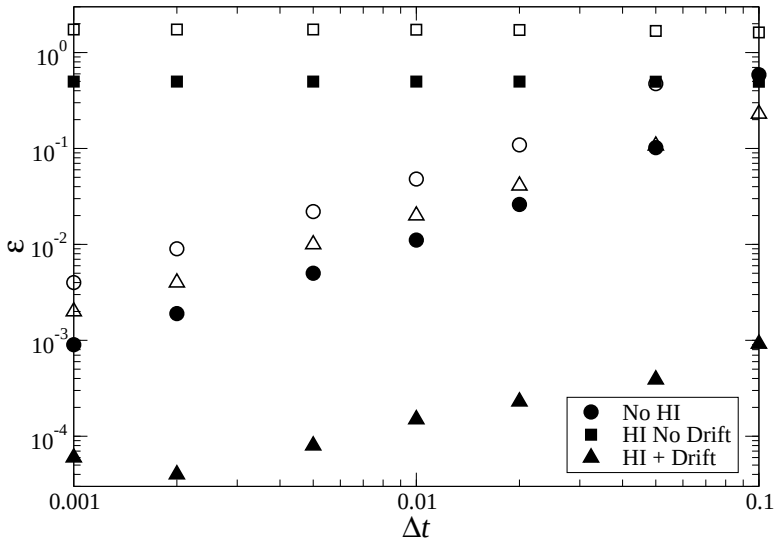

Fig. 1.3. Convergence of the cumulants $\langle q^2 \rangle$ (solid symbols) and $\langle q^4 \rangle$ (open symbols) for a particle near a wall, including hydrodynamic interactions. Numerical results from 10^6 trajectories are compared with the analytic solutions, Eqs. (1.29). Each trajectory was sampled for a time of 100 after an equilibration time of 10. The dimensionless temperature $T = 0.5$. The errors in the cumulants with (triangles) and without (squares) drift correction, are compared with results without HI (circles).

What is most striking in Fig. 1.3 is that FDT is apparently violated when there are hydrodynamic interactions. In the absence of HI, errors in the cumulants decrease linearly in Δt (for small Δt) as before. But with HI the errors in $\langle q^2 \rangle$ and $\langle q^4 \rangle$ remain large, no matter how small the time step.

The problem lies in the reduction of the Langevin equation, Eq. (1.1), to the stochastic differential equation, Eq. (1.4). When the friction is position dependent, there is a contribution from the inertial $\dot{p}$ term in the momentum equation. The full derivation [6] generates an extra "drift" term, which we will discuss in Sec. 1.6, so that the SDE corresponding to the inertialess limit of the Langevin equation, Eq. (1.1), is

$$dq_t = (\beta D_t F_t + D_t')dt + \sqrt{2D_t}dW_t, \tag{1.30}$$

where $F_t = F(q_t)$, $\beta = 1/T$, and D_t' indicates a derivative of the (smooth) function $D(q)$ evaluated at q_t:

$$D_t' = \left(\frac{dD(q)}{dq}\right)_{q_t} \tag{1.31}$$

When the drift correction is included, FDT is recovered, and the moments again converge with decreasing time step (triangles in Fig. 1.3).

1.5 Stochastic calculus – an illustration

It may be helpful in understanding what follows to interject a short introduction to the calculus of stochastic processes. Refs. [14, 21] are an excellent source of theory and applications. As an illustration of some basic ideas, consider the stochastic integral, as defined in Eq. 1.10, of the Wiener process itself,

$$I_t = \int_0^t W_{t'} dW_{t'} = \lim_{n\to\infty} \sum_{i=1}^{n} W_{t_{i-1}} \left(W_{t_i} - W_{t_{i-1}} \right). \tag{1.32}$$

The right-hand side of Eq. (1.32) can be rearranged to give

$$I_t^n = \frac{1}{2} \left[W_{t_n}^2 - \sum_{i=1}^{n} \left(W_{t_i} - W_{t_{i-1}} \right)^2 \right], \tag{1.33}$$

and for large n the summation can be replaced by its expectation value, $\sum_{i=1}^{n} t_i - t_{i-1} = t_n$. Thus the stochastic integral I_t is given by

$$I_t = \int_0^t W_{t'} dW_{t'} = \frac{1}{2} \left(W_t^2 - t \right). \tag{1.34}$$

I_t is called an Itô stochastic integral; the variable X_t, or W_t in this case, is calculated at the beginning of the increment, as shown by the summations in Eqs. (1.10) and (1.32). An Itô process is Markovian, which means that the evolution of X_t after some time t is independent of the history of X up to time t. Note that the Itô integral of W_t has a zero expectation value, $\langle I_t \rangle = 0$.

The Stratanovich integral, $S_t = \int_0^t X_t \circ dW_t$, is defined by taking the value of X_t in the middle of the increment, *c.f.* Eq. (1.10),

$$S_t = \int_0^t X_{t'} \circ dW_{t'} = \lim_{n\to\infty} \sum_{i=1}^{n} \frac{1}{2} \left[X_{t_{i-1}} + X_{t_i} \right] \left(W_{t_i} - W_{t_{i-1}} \right). \tag{1.35}$$

The circle is conventionally used to distinguish Stratanovich and Itô integrals, which are different in general. For example, the Stratanovich integral of the Wiener process, $X_t = W_t$, follows the same integration rule as deterministic calculus,

$$\int_0^t W_{t'} \circ dW_{t'} = \frac{1}{2} W_t^2. \tag{1.36}$$

However, for additive noise the Itô and Stratanovich interpretations coincide.

Exercise 5. Prove Eq. (1.36) *along the lines used for the Itô integral of* W_t*, Eq.* (1.34).

1.6 Fokker-Planck equations

The simple-minded approach used to derive Eq. (1.4) fails when there are hydrodynamic interactions, as in Example 3. To understand what goes wrong we can consider the Fokker-Planck equation that describes the evolution of the probability distribution function, $P(x,t)$, for a stochastic process X_t with multiplicative noise, described by the SDE

$$dX_t = A_t\,dt + B_t\,dW_t. \tag{1.37}$$

Here the coefficients $A_t = A(X_t)$ and $B_t = B(X_t)$ depend only on the stochastic variable X_t; they may also depend explicitly on time, but that complication is not needed here. In terms of the physical problem, $A = \xi^{-1}F$ and $B = \sqrt{2D}$. The Fokker-Planck equation for the probability distribution arising from Eq. (1.37) depends on the choice of the Itô or Stratanovich calculus, because of the different interpretation of the stochastic integral. Here we will use the Itô calculus since the Euler method is a weak first-order approximation to an Itô process.

The Fokker-Planck equation can be derived from the Chapman-Kolmogorov equation for the probability distribution $P(x,t)$ of Markov processes,

$$P(x,t+\Delta t) = \int P(x,\Delta t|x')P(x',t)dx', \tag{1.38}$$

where $P(x,\Delta t|x')$ is the transition probability from x' to x over the time increment Δt. The nature of the Markov process ensures that $P(x,\Delta t|x')$ is independent of t. If Δt is small, then $\Delta x = x - x'$ is also small, and a Kramers-Moyal expansion gives the Fokker-Planck equations for P,

$$\partial_t P(x,t) = \sum_{n=1}^{\infty} \frac{(-1)^n}{n!}\partial_x^n \left[M_n(x)P(x,t)\right], \tag{1.39}$$

where the cumulants are defined in terms of moments of the displacement $\Delta x = x - x'$,

$$M_n(x) = \lim_{\Delta t\to 0}\frac{1}{\Delta t}\int (x-x')^n P(x,\Delta t|x')dx' = \lim_{\Delta t\to 0}\frac{1}{\Delta t}\langle \Delta x^n\rangle. \tag{1.40}$$

Exercise 6. Check the derivation of Eq. (1.39)*. You can verify the key substitution,*

$$P(x,t|x') = \sum_{n=0}^{\infty}\frac{M_n(x')}{n!}(-\partial_x)^n\delta(x-x') \tag{1.41}$$

by taking moments of both sides and integrating by parts.

A stochastic Taylor expansion of the solution to Eq. (1.37), taken to first order in Δt, can to used to evaluate the cumulants in Eq. (1.40):

$$X_{t+\Delta t} = X_t + A_t \Delta t + B_t \left(W_{t+\Delta t} - W_t\right) + B_t B_t' \int_t^{t+\Delta t} \left(W_{t'} - W_t\right) dW_{t'} + \mathcal{O}(\Delta t^{3/2}), \tag{1.42}$$

where $B'(x) = \partial_x B(x)$; a Taylor expansion to first order in Δt needs second-order terms in ΔX_t because of the $\Delta t^{1/2}$ order of the Wiener process. Adopting the Itô interpretation, the first two cumulants are, to order Δt,

$$\langle \Delta X_t \rangle = A_t \Delta t, \, \langle \Delta X_t^2 \rangle = B_t^2 \Delta t, \tag{1.43}$$

since the average value of the integral of the Wiener process is zero, Eq. (1.34). All other moments are of order Δt^2 or higher and so do not contribute in the limit $\Delta t \to 0$.

Exercise 7. Using the integral representation of the SDE,

$$X_{t+\Delta t} = X_t + \int_t^{t+\Delta t} A_{t'} dt' + \int_t^{t+\Delta t} B_{t'} dW_{t'} \tag{1.44}$$

verify the derivation of Eq. (1.42).

From the Kramers-Moyal expansion Eq. (1.39), and the expressions for the moments in Eq. (1.43), the Fokker-Planck equation corresponding to the Itô interpretation of Eq. (1.37) is

$$\partial_t P(q,t) + \partial_q \left[V(q) P(q,t)\right] = \partial_q^2 \left[D(q) P(q,t)\right], \tag{1.45}$$

with a drift velocity $V = A = \xi^{-1} F$ and $D = B^2/2$. However it does not satisfy FDT; in order for the stationary (equilibrium) solution to be Maxwell-Boltzmann, the drift velocity needs an extra term involving the derivative of D,

$$V = \xi^{-1} F + \partial_q D. \tag{1.46}$$

Equation (1.30) is therefore the correct SDE for the Brownian limit of the Langevin equation (using the Itô calculus), with a Fokker-Planck equation

$$\partial_t P(q,t) + \partial_q \left[\xi(q)^{-1} F(q) P(q,t)\right] = \partial_q \left[D(q) \partial_q P(q,t)\right], \tag{1.47}$$

which is the Smoluchowski equation.

Exercise 8. Show that the Fokker-Planck equation, Eq. (1.45)*, with the drift velocity V given by Eq.* (1.46) *leads to a Boltzmann distribution for q at equilibrium (steady state).*

Note that the Stratanovich interpretation of Eq. (1.37) leads to a different Fokker-Planck equation, with a drift velocity $V = A + BB'/2$.

Exercise 9. Use the integral of the Wiener process to calculate the mean drift $\langle X_t \rangle$ for a Stratanovich process, $dX_t = A_t dt + B_t \circ dW_t$.

1.7 Brownian dynamics

The Euler algorithm with the corrected drift velocity, *c.f.* Eq. 1.11,

$$q_{t+\Delta t} = q_t + \left(\xi_t^{-1} F_t + D'_t\right) \Delta t + \sqrt{2D_t \Delta t}\phi_t. \tag{1.48}$$

was derived by a time-ordered expansion of the Langevin equation in a landmark paper by Ermak and McCammon over 30 years ago [6]. It has come to be known as Brownian dynamics, and is one of the most important and frequently cited numerical simulation methods. However there are a number of difficulties with this approach. The most fundamental problem is that it is only first-order accurate and difficult to extend to higher orders. Stochastic Runga-Kutta algorithms are very tricky to derive in the case of multiplicative noise and require many function evaluations, proportional to the number of degrees of freedom in the system. For complicated functions, such as interparticle forces, this is prohibitively expensive. In the next section we will look at an alternative approach, based on an inertial solution of the Langevin equation.

The Ermak-McCammon algorithm is the standard simulation method for polymers, where the hydrodynamic interactions can be approximated by a divergence-free diffusion tensor, thus eliminating the additional drift. However, for more accurate hydrodynamic interactions (for example in Stokesian dynamics), the gradient of the diffusion matrix (in the many-body case) is needed, which is typically not known analytically. However, there is a simple remedy for this, the "Midpoint" method, introduced by Fixman [9]:

$$q_{t+\Delta t/2} = q_t + \frac{1}{2\xi_t}\left(F_t + \sqrt{\frac{2T\xi_t}{\Delta t}}\phi_t\right)\Delta t, \tag{1.49}$$

$$q_{t+\Delta t} = q_t + \frac{1}{\xi_{t+\Delta t/2}}\left(F_t + \sqrt{\frac{2T\xi_t}{\Delta t}}\phi_t\right)\Delta t. \tag{1.50}$$

The Midpoint algorithm is a two step process: first we advance to the middle of the time step and then recompute the mobility. This new "midpoint" mobility is then used to update the coordinate. Note that the conservative force and random force are exactly the same in both steps. It is possible to use the conservative force at the midpoint in the second step, but this does not improve the overall order of the method, because the stochastic term is still only first order. The random force *must* be the same in both steps.

Exercise 10. Use a stochastic Taylor expansion to verify that the Midpoint method generates the correct drift, including the derivative of D.

The Midpoint method recovers first-order convergence, even when there are hydrodynamic interactions (Fig. 1.4). But it has the drawback that it requires a random force, which is then multiplied by the mobility, rather than a random displacement, as in the Euler method. In simulations with many degrees of freedom, for instance a polymer chain, the hydrodynamic

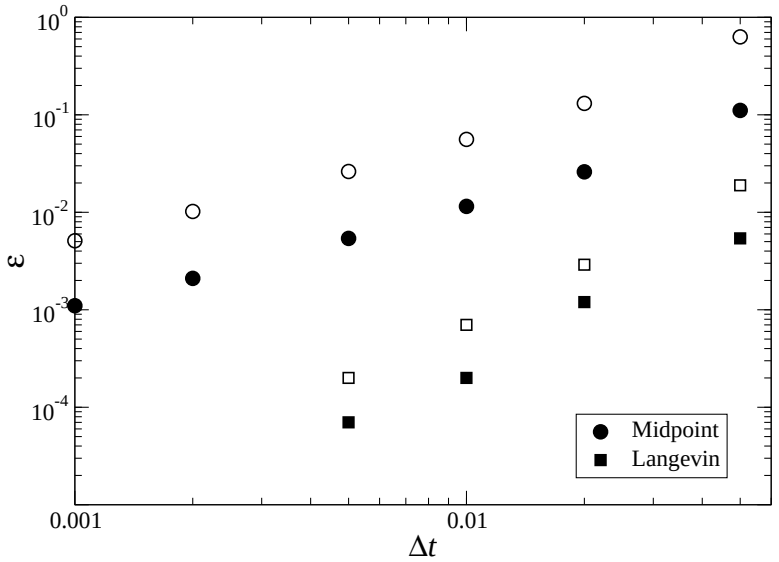

Fig. 1.4. Convergence of the cumulants $\langle q^2 \rangle$ (solid symbols) and $\langle q^4 \rangle$ (open symbols) for a particle near a wall, including hydrodynamic interactions. Numerical results from 10^6 trajectories are compared with the analytic solutions, Eqs. (1.29). Each trajectory was sampled for a time of 100 after an equilibration time of 10. The dimensionless temperature $T = 0.1$. The errors in the cumulants from the Midpoint method (circles) are compared with results from an inertial Langevin simulation (squares).

interactions involve a mobility matrix, which couples all the degrees of freedom together. To use the Midpoint method, this matrix must be inverted, which is an order N^3 operation.

1.8 Langevin dynamics

Brownian dynamics has been the standard method for polymers and dilute colloidal suspensions for many years. The additional inertial time scale needed by a Langevin simulation seems to argue in favor of Brownian dynamics from the standpoint of computational efficiency. Here I want to suggest that the situation is not so obvious and in fact a Langevin simulation may be advantageous, even in the strongly overdamped limit. There are, in fact, several advantages of a Langevin simulation. First, the noise is additive, since the random force is independent of momentum; thus all the complexities and pitfalls of the stochastic calculus are eliminated. Second, it is straightforward to generate explicit second-order algorithms, which need only one function evaluation per time step. Third, a number of mesoscopic algorithms naturally couple the dynamics of particles and fluid on the inertial scale. In Fig. 1.4

we show the convergence of the cumulants for the problem described in Example 3 using the Midpoint method (Sec. 1.7) and a second-order Langevin integrator,

$$\begin{aligned} q^{(1)} &= q_t + \frac{1}{2} v_t \Delta t, \\ v_{t+\Delta t} &= \frac{(1-\alpha^{(1)}/2)v_t + m^{-1}F^{(1)}\Delta t + \sqrt{2m^{-1}T\alpha^{(1)}}\phi_t}{(1+\alpha^{(1)}/2)}, \\ q_{t+\Delta t} &= q^{(1)} + \frac{1}{2} v_{t+\Delta t}\Delta t, \end{aligned} \tag{1.51}$$

where $\alpha^{(1)} = \xi^{(1)}\Delta t/m$ and $F^{(1)}$ are evaluated at $q^{(1)}$. This stochastic version of the Verlet algorithm (SV) will be described in more detail in Sec. 1.12.

The errors in the cumulants are much smaller with SV than Midpoint, and are swamped by the statistical noise for time steps smaller than 0.005. The convergence is second-order in Δt, as opposed to first order for the Midpoint method. Langevin simulations share the disadvantage of the Midpoint method, in that they may need a matrix inversion to calculate the random force, but have the same advantage that no drift correction is needed. Later we will examine the dynamics of simple systems using Midpoint and SV integration to assess the relative computational efficiency in the overdamped case. First we will outline some theory underpinning the development of this class of numerical integrators.

1.9 Symplectic integrators

We have so far focused on establishing the key ideas in the numerical integration of stochastic systems, emphasizing the technical difficulties with applying these techniques to colloids, polymers, and other soft-matter systems. There has been little change in the methodology of Brownian dynamics over the past 30 years; the Ermak-McCammon (or midpoint variant) are used almost exclusively. However a number of alternative methods for modeling hydrodynamic interactions have been proposed that include simplified but explicit models of the solvent; for example lattice-Boltzmann, dissipative particle dynamics, stochastic rotation dynamics and many others; two recent review articles can be found in Refs. [5, 13]. In these models the solute particles are almost always treated as inertial systems, following Eq. (1.1). This has motivated the consideration of Hamiltonian based numerical integrators, adapted to include dissipation and noise [8, 23]. Later on (Secs. 1.13 and 1.18), I will present some results suggesting that these methods may be superior to Brownian dynamics in some instances, even in the overdamped limit. First we must briefly consider some theory underlying the numerical integration of Hamiltonian systems.

When the force is conservative, $F(q) = -\partial_q U(q)$, the dynamics follows Hamilton's equations of motion,

$$\dot{q} = \partial_p H,\ \dot{p} = -\partial_q H, \tag{1.52}$$

where the Hamiltonian $H(q,p)$ is a conserved variable, $\dot{H} = 0$. If we consider a small time increment h, then the new phase point $[Q,P]$ is related to the previous one $[q,p]$ by the approximate formula:

$$Q = q + ph, \tag{1.53}$$
$$P = p + F(q)h, \tag{1.54}$$

taking the mass $m = 1$ for convenience. Any numerical integration step, whether its a simple first-order update as in Eqs. (1.53)–(1.54) or something much more sophisticated, can be regarded as a transformation from one phase point, $[q,p]$ to another, $[Q,P] = [Q(q,p,h), P(q,p,h)]$. The equations of motion at the new phase point can be related to $H(q,p)$, using the equations of motion (1.52):

$$\dot{Q} = (\partial_q Q)(\partial_p H) - (\partial_p Q)(\partial_q H), \tag{1.55}$$
$$\dot{P} = (\partial_q P)(\partial_p H) - (\partial_p P)(\partial_q H). \tag{1.56}$$

A Hamiltonian system tracks a sequence of "canonical" transformations as it evolves in time, which preserve the Hamiltonian form of the equations of motion; in other words

$$\dot{Q} = \partial_P H,\ \dot{P} = -\partial_Q H, \tag{1.57}$$

with H now a function of $[Q,P]$. Using the chain rule to express the derivatives of H in terms of derivatives with respect to q and p, we obtain four conditions which must be satisfied if the transformation from $[q,p]$ to $[Q,P]$ is canonical:

$$\begin{array}{c}(\partial_q Q)_{q,p} = (\partial_P p)_{Q,P},\ \ (\partial_p Q)_{q,p} = -(\partial_P q)_{Q,P} \\ (\partial_q P)_{q,p} = -(\partial_Q p)_{Q,P},\ \ (\partial_p P)_{q,p} = (\partial_Q q)_{Q,P}.\end{array} \tag{1.58}$$

Exercise 11. Show that Eqs. (1.58) *can be written in an equivalent form in terms of the Jacobian matrix,* $M = \partial(Q,P)/\partial(q,p)$*:*

$$\boldsymbol{M}^T \cdot \boldsymbol{S} \cdot \boldsymbol{M} = \boldsymbol{S},\quad \boldsymbol{S} = \begin{bmatrix} 0 & 1 \\ -1 & 0 \end{bmatrix}. \tag{1.59}$$

A numerical integration algorithm that generates a sequence of canonical transformations is called a "Symplectic Integrator"; its trajectories satisfy Eqs. (1.58) or (1.59) exactly for all times. Symplectic integrators maintain a number of invariant properties of the exact dynamics, and this makes them much more stable over long periods of time than standard numerical integrators such as Runga-Kutta or Adams-Bashforth methods. In particular, because the numerical solution remains on the same dynamical subspace as the exact solution, the errors do not increase with time. In section 1.10 we

will use a simple numerical example to examine the benefits of maintaining a symplectic structure.

It is easy to see that the Euler update in Eqs. (1.53)–(1.54) is not symplectic,

$$\boldsymbol{M} = \begin{bmatrix} 1 & h \\ hF'(q) & 1 \end{bmatrix}; \tag{1.60}$$

the triple matrix product in Eq. (1.59) deviates from $\boldsymbol{S}$ by terms of order h^2. However the sequential first-order update,

$$Q = q + ph, \tag{1.61}$$

$$P = p + F(Q)h, \tag{1.62}$$

is symplectic,

$$\boldsymbol{M} = \begin{bmatrix} 1 & h \\ hF'(Q) & 1 + h^2F'(Q) \end{bmatrix}. \tag{1.63}$$

One obvious and important property of symplectic integrators is that they maintain the density of points in the phase space, $\det[\boldsymbol{M}] = 1$. Symplectic integrators do not conserve the Hamiltonian function itself; in fact it is possible to show that no approximate solution can be both energy conserving and symplectic [27]. It is therefore a mistake to try to force exact energy conservation, as is sometimes done in numerical simulations, particularly of continuum systems. However symplectic integrators do conserve a slightly different Hamiltonian H_h, which is the same as H to order h^n, where n is the order of the integrator. This guarantees that the long-time solution cannot be different from the exact solution by terms proportional to t, but only by h^n. We will take a look at how this works out in practice in the next example.

1.10 Example 4: Numerical solutions of a harmonic oscillator

We can investigate the problem of stable long-time integration of Hamiltonian systems through a simple example; the dynamics of a harmonic oscillator with the Hamiltonian (for unit mass, RMS displacement, and energy),

$$H = \frac{1}{2}(p^2 + q^2) = 1. \tag{1.64}$$

Surprisingly, numerical integration of these simple equations of motion, $\dot{q} = p$, $\dot{p} = -q$, is not entirely trivial. Figure 1.5 shows the energy conservation for long-time integration of the oscillator, roughly 10^5 periods, using several different integration methods. First we see that the Euler method is entirely hopeless; despite the small time step, $\Delta t = 10^{-6}$, it cannot maintain energy conservation over more than a few thousand oscillations. It is worth remembering that the standard Brownian dynamics algorithms reduce to the Euler

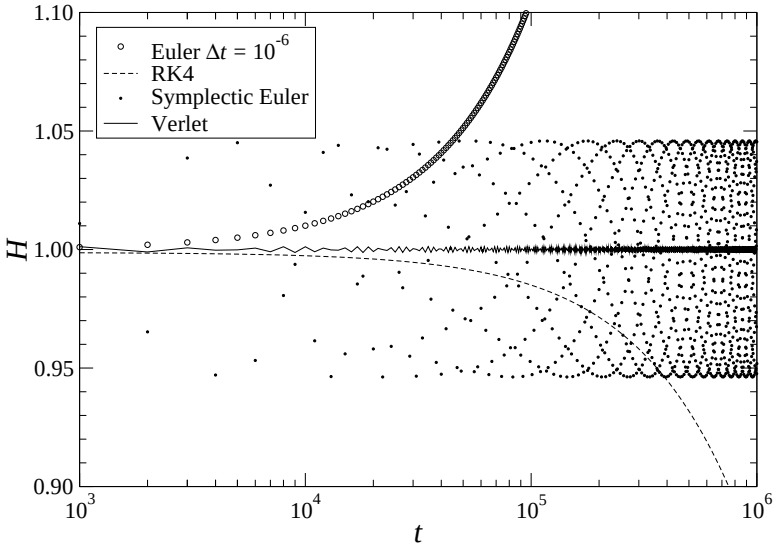

Fig. 1.5. Hamiltonian as a function of time from different numerical integration schemes: Euler method (open circles) with a time step $\Delta t = 10^{-6}$, fourth-order Runga-Kutta (dashed lines), a first-order symplectic method (dots), and the Verlet algorithm (solid line), these last three with $\Delta t = 0.1$.

method in the limit that the frictional force is small. The explicit fourth-order Runga-Kutta method shows the same qualitative behavior, though over significantly larger time scales. Nevertheless, eventually all the energy is dissipated and the oscillator stops at its equilibrium position. By contrast, both symplectic methods maintain approximate energy conservation indefinitely, with no long-term drift. Of course the errors with a second-order, Verlet algorithm,

$$Q = q + ph + \frac{1}{2}F(q + ph/2)h^2, \tag{1.65}$$

$$P = p + F(q + ph/2)h, \tag{1.66}$$

are much smaller than with the first-order method, Eqs (1.61)–(1.62).

As mentioned in the previous section, a symplectic integrator exactly conserves a shadow Hamiltonian, H_h, such that the solutions at time $t = nh$, derived from H_h, exactly match the numerical solution from H at the same time. In general the shadow Hamiltonian can be derived as a power series expansion in h, but for the harmonic oscillator it has a particularly simple form [12],

$$H_h = \frac{p^2}{2m(h)} + \frac{m(h)\omega^2(h)q^2}{2} \tag{1.67}$$

with an effective mass and effective frequency that depend on the integrator and the step size. Expanding m and ω^2 in a power series,

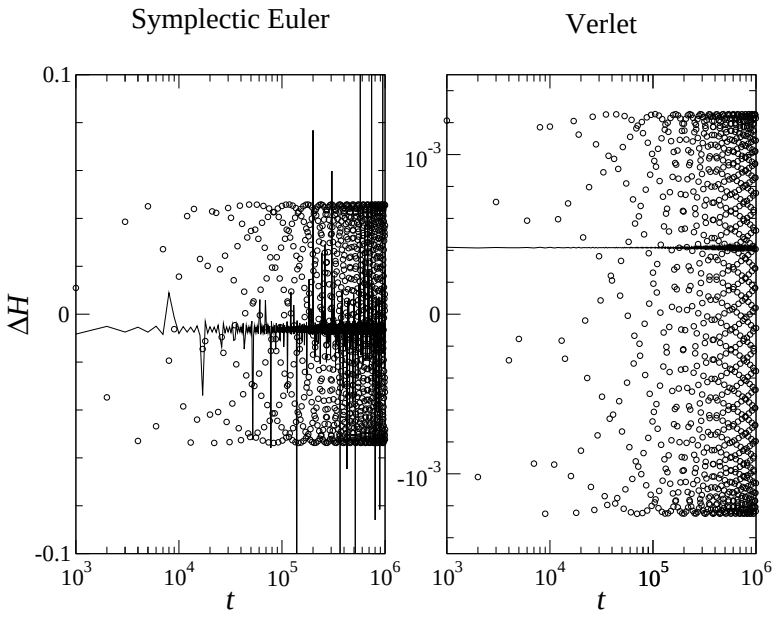

Fig. 1.6. Fluctuations in the Hamiltonian as a function of time from the Symplectic Euler and Verlet integration method. Fluctuations in the Hamiltonian from its initial value, ΔH, are shown as open circles, and fluctuations in the shadow Hamiltonian are shown as solid lines.

$$m(h) = 1 + a_1 h + a_2 h^2 + \ldots, \tag{1.68}$$

$$\omega^2(h) = 1 + b_1 h + b_2 h^2 + \ldots, \tag{1.69}$$

we can match term by term with the approximate solution. The solution of the shadow oscillator at time $t = h$, with initial condition $[q, p]$ is given to order h^2 by

$$q_h = q + ph - q\frac{h^2}{2} - a_1 p h^2 + \mathcal{O}(h^3), \tag{1.70}$$

$$p_h = p - qh - p\frac{h^2}{2} - (a_1 + b_1) q h^2 + \mathcal{O}(h^3). \tag{1.71}$$

Matching coefficients with the 1st-order symplectic update, Eqs. (1.61)–(1.62), gives the first two coefficients a_1 and b_1:

$$a_1 = -\frac{q}{2p},\ b_1 = \frac{p^2 + q^2}{2pq}. \tag{1.72}$$

Exercise 12. Show that for the Verlet algorithm, Eq. (1.65)–(1.66)*, the coefficients to second order are* $a_1 = b_1 = 0$*,* $a_2 = 1/12$*,* $b_2 = 1/12$*.*

The results in Fig. 1.6 show that the shadow Hamiltonian, even with just the first correction in h, is close to being conserved. With the first-order

method, the effective mass and frequency depend on $[q, p]$ and there are occasional large fluctuations in H_h near the zeros of p and q, which show up as spikes in the graph. However, in general, the fluctuations in H_h are an order of magnitude smaller than the fluctuations in H. The Verlet method has constant corrections to the mass and frequency and here the fluctuations in the shadow Hamiltonian ($\mathcal{O}h^2$) are very small; $H_h = 1.00041667(2)$, with fluctuations of ± 2 in the last figure. For more general force laws the shadow Hamiltonian has state dependent coefficients; for the Verlet algorithm [12],

$$H_h = \frac{p^2}{2m} + U(q) + a_2 \frac{p^2 h^2}{2m} F'(q) + (a_2 + b_2) \frac{h^2}{2m} F^2(q), \tag{1.73}$$

where a_2 and b_2 are as given for the harmonic oscillator (Exercise 11). The "velocity Verlet" algorithm,

$$Q = q + ph + \frac{1}{2} F(q) h^2, \tag{1.74}$$

$$P = p + \frac{1}{2} \left[F(q) + F(q + ph + F(q)h^2/2) \right] h, \tag{1.75}$$

has a slightly different shadow Hamiltonian, with $a_2 = -1/6$ and $b_2 = 1/12$. It is worth noting that although the position and momenta lie on a symplectic trajectory, the velocity does not, because of the variation in mass in the shadow Hamiltonian. It has been suggested that a higher order interpolation of the velocity should be used for better energy conservation [12].

1.11 Operator splitting

The earliest symplectic integrators were based on implicit Runga-Kutta methods [22], of which the simplest and most common is the midpoint method,

$$Q = q + \frac{h}{2m} \left[p + P \right], \tag{1.76}$$

$$P = p + \frac{h}{2} \left[F(q) + F(Q) \right]. \tag{1.77}$$

Since Q and P appear on the right-hand side (RHS) of the equations, coupled non-linear algebraic equations must be solved at each time step. This distinguishes implicit integrators from explicit methods where the RHS can be evaluated immediately from q and p. There are no explicit symplectic integrators of the Runga-Kutta type, but Eqs. (1.76)–(1.77) satisfy the symplectic condition, Eq. (1.59), as is easily verified. Nevertheless implicit methods impose a heavy computational burden when the force evaluation is time-consuming, as it typically is in molecular dynamics and related methods. In order to maintain a symplectic integration the algebraic equations must be iterated to machine precision, which typically takes of the order of 10 iterations. Numerical experiments on an elastic filament (Sec. 1.14) show that a modified Verlet

method, derived from operator splitting [4, 18], integrates the equations of motion more accurately for a given time step, and with one-tenth the number of force calculations [16].

Exercise 13. Show that the implicit midpoint method, Eqs. (1.76)–(1.77)*, is symplectic. You will have to solve linear equations to determine an explicit form for the Jacobian (in terms of* q, p*).*

We define the general deterministic propagator $\mathcal{L}$ as

$$\mathcal{L} = \dot{q}\partial_q + \dot{p}\partial_p; \tag{1.78}$$

for Hamiltonian dynamics the time derivatives can be replaced according to the equations of motion, Eq. (1.52). We will see later (Sec. 1.12) how $\mathcal{L}$ can be extended to include random forces. The equation of motion of any dynamical variable $A(q,p)$ can be written in terms of $\mathcal{L}$,

$$\dot{A} = \mathcal{L}A, \tag{1.79}$$

with a formal solution

$$A(q_t, p_t) = e^{\mathcal{L}t}A(q,p) \tag{1.80}$$

Similarly the continuity equation for the phase-space distribution function $f(q,p,t)$,

$$\partial_t f + \mathcal{L}f = 0, \tag{1.81}$$

has the formal solution

$$f(q,p,t) = e^{-\mathcal{L}t}f(q,p,0) \tag{1.82}$$

The key point of operator splitting is that there are many decompositions of $\mathcal{L}$ which result in exactly soluble systems. For example, if we divide $\mathcal{L}$ into a coordinate update $\mathcal{L}^{(q)} = \dot{q}\partial_q$ and a momentum update $\mathcal{L}^{(p)} = \dot{p}\partial_p$, using the superscripts (q) and (p) to indicate the different propagators, then the equations of motion can be integrated exactly, starting from $[q,p]$ in each case:

$$\begin{aligned} q_t^{(q)} &= e^{\mathcal{L}^{(q)}t}q = q + \frac{p}{m}t, \qquad & p_t^{(q)} &= e^{\mathcal{L}^{(q)}t}p = p; \\ q_t^{(p)} &= e^{\mathcal{L}^{(p)}t}q = q, & p_t^{(p)} &= e^{\mathcal{L}^{(p)}t}p = p + F(q)t. \end{aligned} \tag{1.83}$$

The operator $\mathcal{L}^{(q)}$ streams the coordinates at constant momentum, and the operator $\mathcal{L}^{(p)}$ streams the momenta at constant coordinate. If $\mathcal{L}$ corresponds to Hamiltonian dynamics, both these sub-operators do as well, and an exact integration is by definition symplectic (a canonical transformation). Moreover, a sequence of symplectic transformations is also symplectic, and thus we can construct symplectic integrators from any combination of decomposed operators. In the simplest case, we can take

$$e^{\mathcal{L}t} = e^{(\mathcal{L}^{(q)}+\mathcal{L}^{(p)})t} \approx e^{\mathcal{L}^{(p)}t}e^{\mathcal{L}^{(q)}t}, \tag{1.84}$$

which corresponds to a streaming of the positions followed by a momentum update; this is the first-order symplectic Euler method of Eqs. (1.61)–(1.62). Of course one can reverse the order of the operators and obtain another first-order symplectic integrator, with very similar properties.

It is straightforward to derive higher-order integration algorithms by using the Trotter decomposition. Making Taylor expansions of $e^{(\mathcal{L}^{(q)}+\mathcal{L}^{(p)})t}$ and $e^{\mathcal{L}^{(p)}t}e^{\mathcal{L}^{(q)}t}$, remembering that $\mathcal{L}^{(q)}$ and $\mathcal{L}^{(p)}$ do not commute, we see that the expansions are different at second order in t. However the symmetric decomposition

$$e^{\mathcal{L}t} = e^{\mathcal{L}^{(q)}t/2}e^{\mathcal{L}^{(p)}t}e^{\mathcal{L}^{(q)}t/2} + \mathcal{O}(t^3), \tag{1.85}$$

is correct to second order in t and leads to the Verlet algorithm, Eqs. (1.65)–(1.66). Again the operators $\mathcal{L}^{(q)}$ and $\mathcal{L}^{(p)}$ can be exchanged, leading to a different form of the Verlet algorithm, Eqs. (1.74)–(1.75). Higher-order symplectic algorithms can be derived along the same lines, but with multiple force evaluations per time step [11].

Exercise 14. Verify that the approximation in Eq. (1.85) *is correct to second order in* t.

Operator splitting has been used to derive symplectic integrators for rotational motion [4, 18, 28], which has the complication that sequences of rotations do not commute. An exact integration of a finite rotation requires elliptic integrals [28], which are slow to calculate. However rotation about a single axis, is simple to calculate and operator splitting provides the means to combine sequences of rotations with the desired order. A second-order symplectic update of the rotational coordinates, described by $e^{\mathcal{L}^{(q_r)}t}$, can be calculated from five single-axis rotations, $e^{\mathcal{L}_i^{(q_r)}t}$, about three orthogonal axes,

$$e^{\mathcal{L}^{(q_r)}t} = e^{\mathcal{L}_1^{(q_r)}t/2}e^{\mathcal{L}_2^{(q_r)}t/2}e^{\mathcal{L}_3^{(q_r)}t}e^{\mathcal{L}_2^{(q_r)}t/2}e^{\mathcal{L}_1^{(q_r)}t/2} + \mathcal{O}(t^3), \tag{1.86}$$

The update of the rotational coordinates is not exact, but it is symplectic: details can be found in Refs. [4, 18].

Operator splitting is also useful for designing algorithms where the dynamics spans multiple time scales. If $\mathcal{L}^{(F)} = \mathcal{L}^{(q)} + \mathcal{L}^{(p)}$ corresponds to the fast dynamics and $\mathcal{L}^{(S)}$ to a slowly varying force, then a possible second-order multi-step splitting is

$$e^{\mathcal{L}t} = \left(e^{\mathcal{L}^{(F)}t/2M}\right)^M e^{\mathcal{L}^{(S)}t}\left(e^{\mathcal{L}^{(F)}t/2M}\right)^M + \mathcal{O}(t^3), \tag{1.87}$$

where

$$e^{\mathcal{L}^{(F)}t/2M} = \left(e^{\mathcal{L}^{(q)}t/4M}e^{\mathcal{L}^{(p)}t/2M}e^{\mathcal{L}^{(q)}t/4M}\right)^M + \mathcal{O}(t^3). \tag{1.88}$$

The idea is to reduce the number of evaluations of a complex but slowly varying interaction, for example a Coulomb potential. Another example of multi-step splitting is the sequential rotation algorithm, Eq. (1.86), where the rotation, $e^{\mathcal{L}^{(q_r)}t}$, can be broken down into smaller steps, as in Eq. (1.88). A

more accurate integration is obtained without substantial overhead, since no force evaluation is needed [18].

1.12 A Quasi-symplectic integrator for Langevin equations

The Fokker-Planck operator for the Langevin equation, $\mathcal{L}$, can be written as a linear combination of exactly soluble operators:

$$\mathcal{L} = \mathcal{L}_1 + \mathcal{L}_2 + \mathcal{L}_3 + \mathcal{L}_4, \tag{1.89}$$

$$\mathcal{L}_1 = \frac{p}{m}\partial_q, \tag{1.90}$$

$$\mathcal{L}_2 = F(q)\partial_p, \tag{1.91}$$

$$\mathcal{L}_3 = -\frac{\xi(q)}{m}\partial_p p, \tag{1.92}$$

$$\mathcal{L}_4 = -T\xi(q)\partial_p^2. \tag{1.93}$$

$\mathcal{L}_1$ describes the streaming of the particle coordinate at constant velocity, $\mathcal{L}_2$ the update of the momentum by a constant force, $\mathcal{L}_3$ the damping of the momentum by a constant friction, and $\mathcal{L}_4$ the diffusion of momentum needed to satisfy FDT. Note that the derivation of the Fokker-Planck equation in the presence of dissipation is slightly different than in the conservative case, Eq. (1.81). Continuity in phase space gives

$$\partial_t f = -\partial_q(\dot{q}f) - \partial_p(\dot{p}f) = -\mathcal{L}f, \tag{1.94}$$

with the propagator $\mathcal{L}$ as given in Eqs. (1.89)–(1.93). The evolution of dynamical variables is now controlled by a slightly different propagator, $\dot{A} = \tilde{\mathcal{L}}A$, where $\tilde{\mathcal{L}}_3$ is given by

$$\tilde{\mathcal{L}}_3 = -\frac{\xi(q)}{m}p\partial_p. \tag{1.95}$$

Exercise 15. Show that the Maxwell-Boltzmann distribution $f \propto e^{-H/T}$ is a stationary solution of the Fokker-Planck equation $\partial_t f + \mathcal{L}f = 0$.

The sub-operators can be combined in a number of different ways. The stochastic Verlet method, Eqs. (1.51), follows by combining $\mathcal{L}_2$, $\mathcal{L}_3$, and $\mathcal{L}_4$ into a single stochastic momentum equation,

$$dp = F dt - \frac{\xi}{m}p dt + \sqrt{T\xi}\, d\tilde{W}_t \tag{1.96}$$

with the important simplification that F and ξ are constant, so the noise is additive. This equation has an exact solution [25],

$$e^{\mathcal{L}^{(OU)}h}p = p_h = pe^{-\alpha} + \frac{m}{\xi}F(1-e^{-\alpha}) + \sqrt{mT(1-e^{-2\alpha})}\,\phi, \tag{1.97}$$

where $\alpha = \xi h/m$; Eq. (1.97) describes a well-known stochastic process called an Ornstein-Uhlenbeck or OU process. Numerically, the diffusive propagator is replaced by a stochastic process, with $d\tilde{W}_t$ sampled from a discrete distribution that satisfies an appropriate number of moment conditions for the overall accuracy of the integration, Eqs. (1.19)–(1.22). Combining this with the coordinate streaming operator $\mathcal{L}^{(q)}$, Eq. (1.83),

$$e^{\mathcal{L}h} = e^{\mathcal{L}^{(q)}h/2} e^{\mathcal{L}^{(OU)}h} e^{\mathcal{L}^{(q)}h/2} \tag{1.98}$$

gives the stochastic Verlet algorithm, with an Ornstein-Uhlenbeck update of the momentum.

The momentum equation, Eq. (1.96) can be solved approximately by a second-order midpoint method,

$$\frac{p_h - p}{h} = F - \frac{\xi}{2m}(p_h + p) + \sqrt{2T\xi}\,\phi. \tag{1.99}$$

Unlike the case with multiplicative noise (Sec. 1.7), here the midpoint method is second-order accurate. Although Eq. (1.99) is implicit, it is simple to solve for p_h, leading to Eqs. (1.51). The update is exactly the same as an OU process to second order in α, and numerical results are essentially indistinguishable (see Sec. 1.13). The midpoint method can do without the expensive (for q-dependent friction) exponential functions.

There is another obvious combination, which is $\mathcal{L}^{(H)} = \mathcal{L}_1 + \mathcal{L}_2$ describing the conservative dynamics and $\mathcal{L}^{(FD)} = \mathcal{L}_3 + \mathcal{L}_4$ describing dissipation and noise. The operator $\mathcal{L}^{(FD)}$ again describes an OU process, this time without an external force, and can be solved by Eq. (1.97) or Eq. (1.99). The conservative dynamics can be solved with a Verlet algorithm, Eq. (1.85) and the two separate updates must then be wrapped together; for example

$$e^{\mathcal{L}h} = e^{\mathcal{L}^{(FD)}h/2} e^{\mathcal{L}^{(H)}h} e^{\mathcal{L}^{(FD)}h/2}, \tag{1.100}$$

where we placed the force evaluation in the middle so it is only calculated once per step. Normally we would put the most time consuming part of the calculation in the middle so as to evaluate it only once, but if the hydrodynamic part is the most time consuming then the reverse order may be more appropriate;

$$e^{\mathcal{L}h} = e^{\mathcal{L}^{(H)}h/2} e^{\mathcal{L}^{(FD)}h} e^{\mathcal{L}^{(H)}h/2}. \tag{1.101}$$

The frictional dissipation pulls the dynamics from the symplectic surface, but the Jacobian of a finite-time transformation under Langevin dynamics is independent of the configuration in the phase space [19];

$$M = \frac{\partial(Q,P)}{\partial(q,p)} = e^{-\xi h/m}, \tag{1.102}$$

where Q and P are computed *without* the noise term. If the numerical algorithm also has a Jacobean that does not depend on $[q,p]$, and it reduces

to a symplectic method in the limit of vanishing friction, then it is said to be quasi-symplectic. There is a growing body of evidence that such methods are advantageous for integrating stochastic systems [19, 20]. It is worth noting that although it is straightforward to derive higher-order integrators for Hamiltonian dynamics [11], in Langevin systems operator splitting cannot be extended beyond second-order [24], but requires additional commutators [10].

Exercise 16. Show that these algorithms, Eqs. (1.98)*,* (1.100)*, and* (1.101)*, are quasi-symplectic. Note that Eq.* (1.101) *is more complicated to prove than the other two.*

A multi-step splitting is frequently needed to couple a coarse-grained molecular solute, for example a polymer, to a solvent. Here the hydrodynamic interactions change much more slowly than the interparticle forces, but are much more time consuming to calculate [5]. A recent implementation, based on the splitting in Eq. (1.101), but allowing for the possibility of splitting the conservative dynamics into a number of smaller sub cycles (1.87),

$$e^{\mathcal{L}h} = \left(e^{\mathcal{L}^{(H)}h/2M}\right)^M e^{\mathcal{L}^{(FD)}h} \left(e^{\mathcal{L}^{(H)}h/2M}\right)^M, \tag{1.103}$$

was implemented recently in the context of polymers coupled to a fluctuating lattice-Boltzmann model [15].

1.13 Example 3 revisited: Operator splitting

Having seen how an explicit symplectic integrator works for Hamiltonian systems, we now explore applications to Langevin dynamics, which become Hamiltonian in the limit that the friction is small. However, our primary concern is the overdamped regime where we can compare with Brownian dynamics. We will again consider the problem of a particle near a plane wall, as in Example 3 (Sec. 1.4), with an interaction potential

$$\phi = \epsilon \left[\frac{1}{2}\left(\frac{q}{\bar{q}}\right)^2 - \ln\left(\frac{q}{\bar{q}}\right)\right], \tag{1.104}$$

where $\bar{q}$ is the equilibrium position in the non-linear trap formed by the wall repulsion and the harmonic spring force. In Sec. 1.4 we took $\bar{q} = 1$ and $\epsilon = 1$. In a system of reduced units, scaling length by the mean position in the trap and time by the frequency of the trap, $\omega^2 = \epsilon/m\bar{q}^2$, the Langevin equation for this system can be written as

$$\dot{q}^\star = v^\star, \tag{1.105}$$

$$\dot{v}^\star = -\frac{v^\star}{m^\star q^\star} + \left(q^{\star -1} - q^\star\right) + \sqrt{\frac{2D^\star}{q}}\phi(t^\star). \tag{1.106}$$

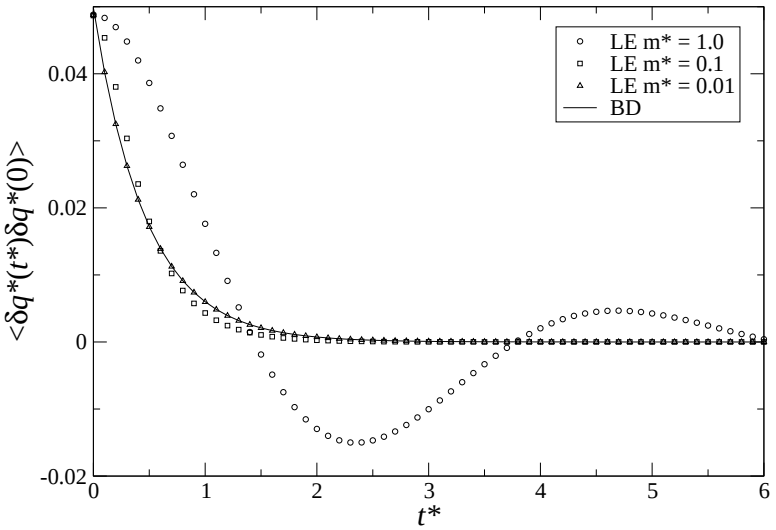

Fig. 1.7. Autocorrelation function of the particle position. Comparison of Langevin dynamics, Eqs. (1.85) and (1.99) with Brownian dynamics (BD), Eqs. (1.49)–(1.50). The Langevin equation (LE) has been solved with $D^\star = 0.1$ and for different reduced masses, $m^\star$. The time steps for the various simulations were chosen for convergent results: LE $m^\star = 1.0$ $\Delta t^\star = 0.1$, LE $m^\star = 0.1$ $\Delta t^\star = 0.1$, LE $m^\star = 0.01$ $\Delta t^\star = 0.02$, BD $\Delta t^\star = 0.02$.

The reduced mass $m^\star = m\omega/\xi_0$, the effective diffusivity $D^\star = T\xi_0^{-1}(m^\star\omega\bar{q})^{-2}$, and $\xi_0 = 6\pi\eta a^2/\bar{q}$. By integrating the Langevin equation directly, we automatically account for the diffusional drift term that shows up in the inertialess simulation, Eq. (1.30).

Figure 1.7 shows the autocorrelation function $\langle \delta q^\star(t)\delta q^\star(0)\rangle$ of the fluctuations in position $\delta q^\star = q^\star - 1$ for a range of effective mass, $m^\star$. For $m^\star = 1$ we are in the underdamped regime, with oscillations in the correlation function as the particle bounces back and forth in the trap. The Brownian limit is approached when $m^\star < 0.1$ and for $m^\star < 0.01$ the correlation functions from Langevin and Brownian dynamics are statistically indistinguishable. Somewhat surprisingly the additional inertial time scale does not translate to a significantly smaller time step for Langevin dynamics compared with Brownian dynamics; in both cases $\Delta t^\star = 0.02$. However the time step is set by rather different requirements. In the case of the Langevin simulations there is an upper limit to the time step in order to prevent the particle crossing the wall. For $m^\star = 0.01$ we found occasional crossings with $\Delta t^\star = 0.05$, although with more inertia a larger time step can be used. In Brownian dynamics, Eqs. (1.49)–(1.50), the primary limitation is the accuracy of the initial fluctuations in position, which requires a time step of the order of 0.01 for 1% accuracy (see Fig. 1.3).

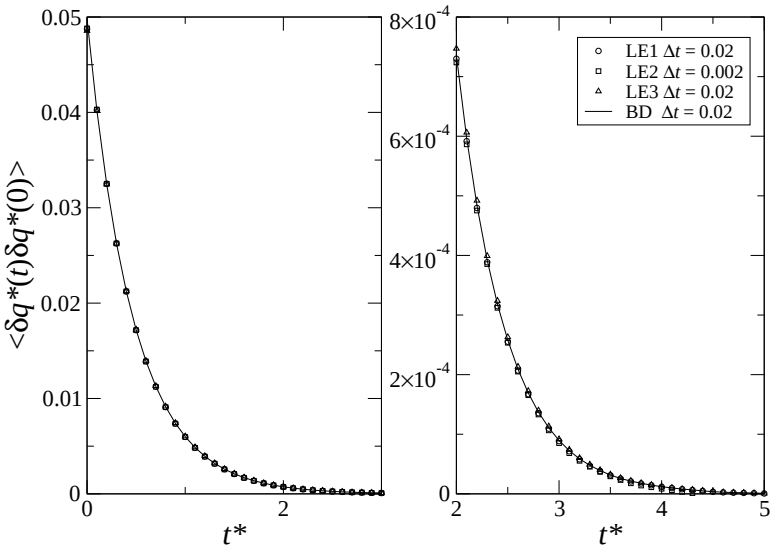

Fig. 1.8. Autocorrelation function of the particle position in the inertialess limit. Comparison of Langevin dynamics, Eqs. (1.85) and (1.99) with Brownian dynamics, Eqs. (1.49)–(1.50). The Langevin equation has been solved with $D^\star = 0.1$ and $m^\star = 0.01$.

Simulations based on the position-momentum decomposition, Eq. (1.85), led to the most accurate results for a given $\Delta t^\star$. We found no discernible difference between the Ornstein-Uhlenbeck update of the momentum, Eq. (1.97), and the midpoint update, Eq. (1.99). However, Eq. (1.85) was also the most prone to wall crossings at larger values of the time step. In Fig. 1.8 we compare correlation functions in the inertialess limit ($m^\star = 0.01$) for the three different splittings, Eq. (1.85), Eq. (1.100), and Eq. (1.101), using the midpoint momentum update, Eq. (1.99) in each case. Essentially identical results are obtained in each case, in excellent agreement with Brownian dynamics. We note than one of the splittings, denoted LE2 in Fig. 1.8 and corresponding to Eq. (1.100), requires a time step that is about an order of magnitude smaller than the other methods. The relatively poor convergence of this splitting has been noticed in other work as well [10]. The LE3 method, Eq. (1.101), can use a larger time step without generating wall crossings, presumably because the conservative dynamics is integrated twice as often, but it is slightly less accurate than the stochastic Verlet splitting, Eq. (1.85). For cases where the force calculation dominates the computation, the stochastic Verlet method seems the most suitable.

Interestingly, there is no advantage to Brownian dynamics in terms of accuracy for a given time step. To the contrary, if zero-time fluctuations are needed, the inertial methods do much better at less cost. However, Brownian dynamics has a significant advantage in that it uses the mobility tensor,

which can be calculated by direct summation, rather than the friction tensor, which requires a matrix inversion. In the simplified Rotne-Prager interaction, commonly used for polymer simulations, the divergence of the mobility tensor vanishes; there is no drift correction to calculate and the Euler method can be used directly. However, if there is drift, then the friction matrix is needed to implement the midpoint method. Moreover, with more complicated hydrodynamic interactions, such as lubrication forces, the friction matrix is needed anyway. In such instances, an inertial simulation may be simpler and more efficient. The application of inertial simulations to the Brownian limit perhaps warrants more consideration than it has so far received.

1.14 Elastic filaments

In the remainder of these notes I will examine numerical integration methods for continuum equations of motion in which there is also an underlying Hamiltonian structure. We will consider a single example, namely elastic rods or filaments; the material is adapted from Ref. [16], which can be consulted for further details. Elastic filaments, long, thin, flexible rods, are a model for a wide range semi-flexible polymers, such as DNA, actin, and microtubules. The key parameter is the persistence length, l_p, which characterizes the length over which the filament, in thermal equilibrium, loses memory of its direction. On the biological scale ($1\mu m$), DNA, with a persistence length of $150nm$, is flexible, actin, with a persistence length of $15\mu m$ is semiflexible, and microtubules, with persistence lengths of the order of $1mm$ are rigid. The mechanical properties of the cytoskeleton depend on a complex interplay between filamentous proteins, such as actin and tubulin, cross-linking molecules such as α-actinin and formalin, and ATP-driven motor proteins, such as myosin and dynein. Numerical simulations of cell mechanics will require reliable means to integrate the equations of motion of elastic bodies, such as membranes and filaments. Here we consider the simplest problem, a one-dimensional flexible filament.

An elastic filament (or thin rod) is described by the coordinates of its centerline $\boldsymbol{r}(s)$ and a set of orthonormal directors $\boldsymbol{d}_1(s)$, $\boldsymbol{d}_2(s)$, $\boldsymbol{d}_3(s)$. The directors establish the orientation of a cross section or material plane at the location s, where s is a parametric coordinate defining the position of each point along the centerline. In the undeformed filament, s is the contour length from the origin. We will choose a body-fixed coordinate system such that $\boldsymbol{d}_1$ and $\boldsymbol{d}_2$ point along the principal axes of inertia of the cross section and therefore $\boldsymbol{d}_3 = \boldsymbol{d}_1 \times \boldsymbol{d}_2$ is normal to the material plane; the coordinate system is illustrated in Fig 1.9.

The key assumption of thin-rod elasticity is that there is no deformation within a material plane, only translation and rotation of that plane. Then the equations of three-dimensional elasticity can be reduced to equations for 6 one-dimensional strain fields, $\boldsymbol{\Gamma}(s)$ and $\boldsymbol{\Omega}(s)$,

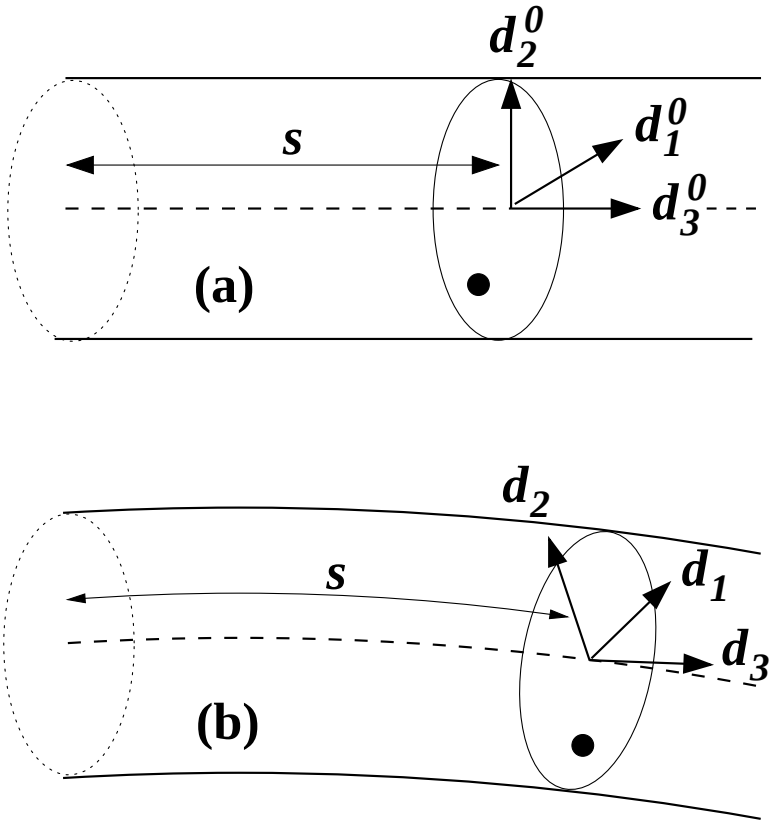

Fig. 1.9. An elastic filament in the unstrained (reference) state (a) and after deformation (b). In the reference state, the material plane, shown by the solid ellipse, is aligned with its normal parallel to the tangent to the centerline (dashed line). The local director basis of the reference state, $\boldsymbol{d}_i^0(s)$, and the deformed state, $\boldsymbol{d}_i(s)$, are also shown. A material point (solid black circle) moves with the translation and rotation of the local coordinate system; in this case extension, shear, bend, and twist can all be seen.

$$\begin{array}{ll} \Gamma_1 = \boldsymbol{d}_1 \cdot (\partial_s \boldsymbol{r}) & \Omega_1 = \boldsymbol{d}_3 \cdot (\partial_s \boldsymbol{d}_2) = -\boldsymbol{d}_2 \cdot (\partial_s \boldsymbol{d}_3) \\ \Gamma_2 = \boldsymbol{d}_2 \cdot (\partial_s \boldsymbol{r}) & \Omega_2 = \boldsymbol{d}_1 \cdot (\partial_s \boldsymbol{d}_3) = -\boldsymbol{d}_3 \cdot (\partial_s \boldsymbol{d}_1) \\ \Gamma_3 = \boldsymbol{d}_3 \cdot (\partial_s \boldsymbol{r}) & \Omega_3 = \boldsymbol{d}_2 \cdot (\partial_s \boldsymbol{d}_1) = -\boldsymbol{d}_1 \cdot (\partial_s \boldsymbol{d}_2). \end{array} \tag{1.107}$$

Γ_1 and Γ_2 describe transverse motions of a material plane with respect to the normal vector ($\boldsymbol{d}_3$), which causes shearing of the segment, while Γ_3 describes extension or compression of the segment. Bending of the segment about its principal axes is described by Ω_1 and Ω_2, and twisting of the segment by Ω_3. For example, a helical rod can be described by a constant bend and twist, $\boldsymbol{\Gamma} = [0, 0, 1]$, $\boldsymbol{\Omega} = [R\kappa^2, 0, P\kappa^2]$, where R is the radius of the helix, $2\pi P$ is the pitch, and the combined curvature due to bend and twist, $\kappa = (P^2 + R^2)^{-1/2}$. The

choice of signs define a right-handed helix, $\boldsymbol{r}(s) = [R\cos(\kappa s), R\sin(\kappa s), P\kappa s]$, with basis vectors

$$\begin{aligned} \boldsymbol{d}_1 &= [P\kappa\sin(\kappa s), -P\kappa\cos(\kappa s), R\kappa] \\ \boldsymbol{d}_2 &= [\cos(\kappa s), \sin(\kappa s), 0] \\ \boldsymbol{d}_3 &= [-R\kappa\sin(\kappa s), R\kappa\cos(\kappa s), P\kappa]. \end{aligned} \tag{1.108}$$

The equations of motion of the elastic rod have a Hamiltonian form, where H is now a line integral over the curve $\boldsymbol{r}(s)$,

$$H = \int_0^L \sum_{i=1}^{3} \left(\frac{p_i^2}{2M} + \frac{l_i^2}{2I_i} + \frac{C_i^{\Gamma}}{2}(\Gamma_i - \Gamma_i^0)^2 + \frac{C_i^{\Omega}}{2}(\Omega_i - \Omega_i^0)^2 \right) ds; \tag{1.109}$$

p_i and l_i are the linear and angular momenta densities in the body-fixed frame of a material segment with mass density M and moments of inertia I_i. Thus, for example, the linear momentum of small segment, bounded by the material planes s and $s + ds$, is $\boldsymbol{p}ds$ and the mass is Mds. C_i^{Γ} and C_i^{Ω} are elastic constants, and $\boldsymbol{\Gamma}^0$ and $\boldsymbol{\Omega}^0$ are the strains in the reference configuration. If the undeformed rod is straight, $\boldsymbol{\Gamma}^0 = [0, 0, 1]$, $\boldsymbol{\Omega}^0 = [0, 0, 0]$. The form of H is deceptively simple, yet it describes a very stiff non-linear system, as we shall see.

The equations of motion follow by functional differentiation. Imagine a small variation in the position of the centerline $\delta\boldsymbol{r}(s)$; the change in the Hamiltonian, δH, is

$$\delta H = \int_0^L \sum_{i=1}^{3} F_i^{\Gamma} \boldsymbol{d}_i \cdot \delta\boldsymbol{r}' ds, \tag{1.110}$$

where $F_i^{\Gamma} = C_i^{\Gamma}(\Gamma_i - \Gamma_i^0)$ is the force (integrated stress) on the material plane and $\boldsymbol{r}' = \partial_s \boldsymbol{r}$. The forces (and couples) are simplest in the body frame, giving Eq. (1.109) its simple structure, while the variations in position must be in the space-fixed frame. The two frames are connected by the rotation matrix or set of basis vectors $\boldsymbol{d}_i$. Integrating by parts, we obtain the equation of motion for the linear momentum by functional differentiation,

$$\dot{\boldsymbol{p}} = -\frac{\delta H}{\delta r} = \partial_s \boldsymbol{F}^{\Gamma}. \tag{1.111}$$

A similar but more involved calculation [16] gives the equation of motion for the angular momentum

$$\dot{\boldsymbol{l}} = \partial_s \boldsymbol{F}^{\Omega} + \boldsymbol{r}' \times \boldsymbol{F}^{\Gamma}, \tag{1.112}$$

where the couples (in the body-fixed frame) are given by $F_i^{\Omega} = C_i^{\Omega}(\Omega_i - \Omega_i^0)$. Note that these equations of motion have been written in the space-fixed frame; in the body-fixed frame there are additional components from the rotation of the frame.

The important distinction between the equations of motion shown in Eqs. (1.111)–(1.112) and the classical Kirchoff model is that here we have explicitly modeled the shear and extensional forces $\boldsymbol{F}^{\Gamma}$ in terms of the corresponding strain fields. In the Kirchoff model, it is argued (correctly of course) that the shear and extensional *strains* are small and can be safely neglected, leaving $\boldsymbol{F}^{\Gamma}$ as an implicitly determined constraint force. To see how this works, we will consider the simplest variant of the Kirchoff model, neglecting the angular momentum about the bending axes, the so-called "rotatory inertia"; the point is the same in the more general case. The tangent vector $\partial_s \boldsymbol{r}$ is now identical to $\boldsymbol{d}_3$ ($\boldsymbol{\Gamma} = \boldsymbol{\Gamma}_0$) and the shear forces $\boldsymbol{F}^{\Gamma,\perp}$, are constrained by the angular momentum balance, Eq. (1.112),

$$\boldsymbol{d}_3 \times \partial_s \boldsymbol{F}^{\Omega} = (\mathbf{1} - \boldsymbol{d}_3 \boldsymbol{d}_3) \cdot \boldsymbol{F}^{\Gamma} = \boldsymbol{F}^{\Gamma,\perp}. \tag{1.113}$$

The constraint force F_3^{Γ} is determined from the inextensibility condition,

$$\partial_s \boldsymbol{r} \cdot \partial_s \boldsymbol{r} = 1. \tag{1.114}$$

The Kirchhoff model has the computational advantage that the shear and extensional modes are frozen by the constraints, so that a larger time step may be used. On the other hand the numerical integration is inherently implicit and must be solved iteratively at each time step.

Bending forces can also be determined from the curvature in the centerline position vector, $\boldsymbol{r}' \times \boldsymbol{r}''$, rather than from derivatives of the basis vectors, Eq. (1.107). In the case of a weakly bent filament, the tangent can be assumed to be locally constant and, with an isotropic bending stiffness $C_1^{\Omega} = C_2^{\Omega} = C^{\Omega}$,

$$\boldsymbol{F}^{\Gamma,\perp} = -C^{\Omega} (\mathbf{1} - \boldsymbol{r}'\boldsymbol{r}') \cdot \boldsymbol{r}'''. \tag{1.115}$$

Differentiating once more (again ignoring derivatives of $\boldsymbol{r}'$), we obtain the equation of motion for the bending of a worm-like-chain (WLC) model,

$$M\ddot{\boldsymbol{r}} = -C^{\Omega} (\mathbf{1} - \boldsymbol{r}'\boldsymbol{r}') \cdot \boldsymbol{r}''''. \tag{1.116}$$

Unfortunately, Eq. 1.116 is very stiff, and numerical integration of the partial differential equations is not straightforward. Most simulations of the WLC model have therefore discretized the filament into a sequence of beads interacting via a bending potential [7, 26, 17]. Although this sacrifices fidelity to the continuum filament model, the ordinary differential equations for the bead positions can be integrated using standard molecular dynamics (MD) methods, including constraint forces to maintain a discrete approximation to Eq. (1.114). In the next section (Sec. 1.15) I will describe how the full elastic equations can be reduced to an MD like simulation, taking advantage of a symplectic integrator to ensure long-term stability.

1.15 Numerical integration of the equations of motion of an elastic filament

I will not go in specifics about the numerical algorithm here, but simply outline the key ideas; further details can be found in Ref. [16]. The filament is divided into N equal segments of length $\Delta s = L/N$, and nodes are defined at the center of each segment [3],

$$s_n = \left(n - \tfrac{1}{2}\right) \Delta s, \quad n = 1, 2, \ldots N. \tag{1.117}$$

The instantaneous state of the filament is then given by the nodal coordinates $\boldsymbol{r}^n$, quaternions $\boldsymbol{q}^n$, linear momenta $\boldsymbol{p}^n$, and angular momenta $\boldsymbol{l}^n$. We use quaternions in preference to the director basis vectors since it reduces the number of degrees of freedom. Symplectic integration algorithms using operator splitting exist for both quaternions [18] and director vectors [4]. Key properties of quaternions are summarized in the Appendix to Ref. [16].

Derivatives $\boldsymbol{r}'^n$ are approximated by centered differences at the discrete locations $n\Delta s$, midway between the nodes,

$$\boldsymbol{r}'^n = \frac{\boldsymbol{r}^{n+1} - \boldsymbol{r}^n}{\Delta s} + \mathcal{O}(\Delta s)^2, \tag{1.118}$$

and the elastic forces at the interior positions $n\Delta s$, $n = 1, 2, \ldots, N-1$, are then

$$\boldsymbol{F}^{\Gamma,n} = \sum_{i=1}^{3} C_i^{\Gamma} \bar{\boldsymbol{d}}_i^n \left(\bar{\boldsymbol{d}}_i^n \cdot \boldsymbol{r}'^n - \Gamma_i^0\right). \tag{1.119}$$

where the notation $\bar{\boldsymbol{d}}_i^n$ indicates the midpoint basis vectors are calculated by averaging the nodal quaternions on either side. The forces at the ends of the rod, $n = 0$ and $n = N$, are determined by the boundary conditions; for free ends,

$$\boldsymbol{F}^{\Gamma,0} = \boldsymbol{F}^{\Gamma,N} = 0, \tag{1.120}$$

A nice feature of the midpoint discretization [3] is that the strains are naturally evaluated at integer multiples of the segment length, $n\Delta s$, with $n = 0, 1, \ldots, N$. An additional differencing of the internal forces and couples then gives accelerations back at the nodal positions. Thus the algorithm is second-order accurate in Δs, with only three nodes directly interacting with one another, just as in the worm-like-chain model. The nodal coordinates and momenta satisfy the ordinary differential equations ($n = 1, 2, \ldots, N$)

$$\dot{r}_\alpha^n = \frac{p_\alpha^n}{M}, \tag{1.121}$$

$$\dot{p}_\alpha^n = \frac{F_\alpha^{\Gamma,n} - F_\alpha^{\Gamma,n-1}}{\Delta s}. \tag{1.122}$$

Equations of motion for the quaternions and angular momenta follow in similar fashion, but are somewhat more involved; again, details are in Ref. [16].

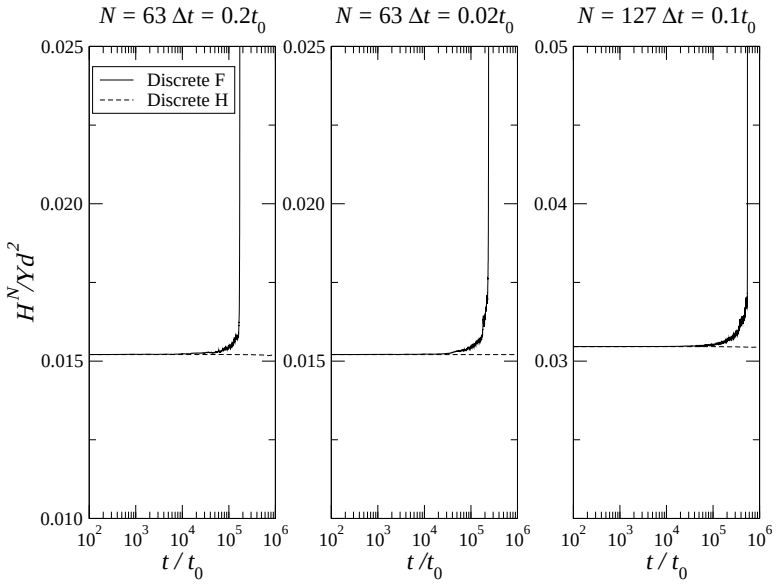

Fig. 1.10. Conservation of energy for discrete force and discrete Hamiltonian dynamics: a) 63 segments, $\Delta t = 0.2t_0$; b) 63 segments, $\Delta t = 0.02t_0$; c) 127 segments, $\Delta t = 0.1t_0$.

1.16 Example 5. Dynamics of a uniformly bent filament

We investigated the stability of the numerical method using a simple two-dimensional test problem. A straight filament of length $20\pi d$ was bent into a circle of radius $10d$ and released. The dynamics were followed for two different spatial discretizations, dividing the filament into 63 or 127 equal segments; the corresponding segment lengths were approximately d and $0.5d$. We used a generalization of the Verlet method, outlined in Sec. 1.9 and described in detail in Refs [4, 18, 16]. The filament unwinds from its initially circular configuration in a highly non-linear fashion, with transitions through a surprising variety of shapes [16]. The motion is roughly periodic; a complete cycle takes about $6000t_0$ for a filament of length $L \sim 60d$, and is quadratic in the length of the filament. Here the unit of time $t_0 = d/c_l$, where c_l is the longitudinal wave speed. A plot of energy *vs.* time, Fig. 1.10a, shows that the spatially discretized equations (1.121)–(1.122) integrate stably for about 10 oscillations, but after that the energy diverges. The instability is unaffected by a reduction in time step, Fig. 1.10b; it is delayed, but not averted, by a reduction in the segment length, Fig. 1.10c. This suggests that the problem is with the formulation of the equations of motion themselves.

1.17 Hamiltonian formulation

Integrating the equations of motion of an elastic filament is a long-standing problem in numerical continuum mechanics. Many solutions, most of them complicated have been proposed, but the most obvious solution, ensuring the Hamiltonian structure of the discretized equations, has only been followed occasionally [3]. Typical finite-difference or finite element discretizations of the continuum equations of motion (1.111)–(1.112) do not preserve the underlying Hamiltonian structure. Thus the discrete equations of motion, Eq. (1.121)–(1.122) are only Hamiltonian in the limit $\Delta s \to 0$. At any finite discretization, the symplectic structure of the continuum equations is lost and so the energy is not well conserved. Of course more accurate discretizations, coupled with techniques to suppress instabilities can extend the range of integration time. But a simple and more complete solution is to ensure that the discrete equations of motion are themselves Hamiltonian. Then a symplectic time integration algorithm will conserve energy essentially indefinitely, as we have seen.

Once this point is realized, the implementation is straightforward, using a second-order quadrature to approximate the line integral in Eq. (1.109). The kinetic energy can be approximated by the midpoint rule,

$$T^N = \sum_{n=1}^{N} \left(\frac{\boldsymbol{p}^n \cdot \boldsymbol{p}^n}{2M} + \frac{\boldsymbol{l}^n \cdot \boldsymbol{l}^n}{2I_i} \right), \tag{1.123}$$

where $\mathcal{T}^N$ is the discrete kinetic energy per unit length. Equation 1.123 is a second order approximation to the kinetic energy of the continuous filament, $\mathcal{T} = \mathcal{T}^N \Delta s + \mathcal{O}(\Delta s)^3$. Discrete approximations to the potential energy involve coordinate differences evaluated at the midpoints between pairs of nodes. We therefore used the trapezoidal rule to approximate the potential energy, which is also second order in Δs,

$$U^N = \frac{1}{2} \sum_{m=1}^{N-1} \left[C_i^{\Gamma} |\bar{\boldsymbol{\Gamma}}^m - \bar{\boldsymbol{\Gamma}}^{0,m}|^2 + C_i^{\Omega} |\boldsymbol{\Omega}^m - \boldsymbol{\Omega}^{0,m}|^2 \right]. \tag{1.124}$$

The strains are evaluated at the midpoints between the nodes and for free boundary conditions there are no contributions from the ends of the rod ($m = 0$, $m = N$). The equations of motion for the nodal coordinates and momenta then follow by differentiation of the Hamiltonian $H^N = T^N + U^N$. It is essential that the differentiation is done exactly or the Hamiltonian structure of the discrete equations is lost. The improvement in energy conservation is clearly seen in Fig. 1.10 where the energy is conserved for as long as we have integrated, up to $10^8 t_0$.

The computational efficiency of explicit operator splitting (OS), Eq. (1.85), can be compared with the performance of the implicit midpoint method (MP), Eqs. (1.76)–(1.77). The short-time fluctuations in energy of the OS algorithm cannot be seen on the scale of Fig. 1.10, but they are quadratic in the time

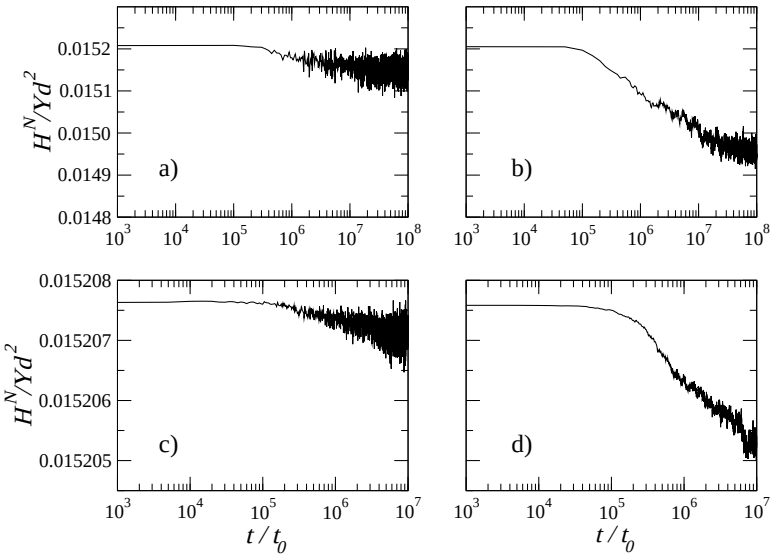

Fig. 1.11. Conservation of energy for second-order symplectic algorithms derived from operator splitting (OS) and the implicit midpoint (MP) methods; 63 segments were used in each case. a) OS, $\Delta t = 0.2t_0$; b) MP $\Delta t = 0.2t_0$; c) OS, $\Delta t = 0.02t_0$; d) MP, $\Delta t = 0.02t_0$. Y is the Young's modulus of the filament and d is its diameter.

step, with a relative magnitude of approximately $0.1(\Delta t/t_0)^2$. These short-time fluctuations in energy are about 20 times larger with OS than with MP. However there is also an initial drift in the energy, again quadratic in Δt, but larger, as shown in Fig. 1.11. Over long time intervals, OS preserves energy conservation with about an order of magnitude better accuracy than MP at the same Δt (Fig. 1.11). MP requires 5-10 times as many force evaluations per time step as OS, so the explicit operator splitting algorithm is clearly preferable for long-time dynamics.

Dichmann and Maddocks studied the dynamics of a Kirchhoff rod from the same initial configuration [3], but with the filament pinned at one end. The nodal forces and torques were also Hamiltonian, but the implicit midpoint integrator was used instead of operator splitting. Their results showed a small drift in the total energy of around 0.2% after approximately 30 oscillations of the filament, or $200,000t_0$ in our units. Our rod model requires a smaller time step to explicitly integrate the shear and extensional degrees of freedom, but surprisingly, it is only a factor of 8 smaller than the time step used for the constrained rod. Since the implicit midpoint method requires 5-10 function evaluations per time step, the fully explicit method can integrate the complete rod model, including shear and extension, with about the same computational cost as an implicit integration of the Kirchhoff model. If excluded volume interactions are included, it is likely that these very stiff forces

will set the overall time step, as is typical in molecular dynamics simulations. In such cases the computational advantages of a fully explicit simulation will be considerable.

1.18 Thermal fluctuations in elastic filaments

The dynamics of a Hamiltonian rod can be extended to include Brownian motion by adding an appropriate dissipation and noise to the linear and angular momentum equations. Since the friction coefficients depend on the local orientation of the segment, it is simplest to write the equations of motion in the body-fixed frame. For example, the equation for the linear momentum of a segment is

$$\dot{p}_i = \frac{(\boldsymbol{F}^{\Gamma,n} - \boldsymbol{F}^{\Gamma,n-1})}{\Delta s} \cdot \boldsymbol{d}_i - \xi_i p_i + \sqrt{2mT\xi_i}\,\phi_i. \tag{1.125}$$

Expressions for the friction coefficients of a cylindrical rod can be found in Refs. [1, 2]. In deriving Eq. (1.125) we have made implicit use of the Trotter decomposition, which allows us to update the momentum with the coordinates held fixed. Otherwise we would have to consider the rotation of the frame as well, which would complicate things considerably.

At the time of writing, this is still an active area of research and I will only offer a brief summary of our findings with regard to the numerical integration. We have investigated the extent of equipartition between the various degrees of freedom as a first investigation of the accuracy of the integration method. The quadratic form of the Hamiltonian, Eq. (1.109), means that the kinetic and potential energies in each of the six degrees of freedom, corresponding to fluctuations in $\boldsymbol{\Gamma}$ and $\boldsymbol{\Omega}$ should show equipartition of energy in the continuum limit. We have measured the mean deviations in strain energy,

$$\alpha_i = \sum_{m=1}^{N-1} \frac{\left(\Gamma_i^n - \Gamma_i^{0,n}\right)^2}{M(N-1)T} - 1, \tag{1.126}$$

$$\beta_i = \sum_{m=1}^{N-1} \frac{\left(\Omega_i^n - \Omega_i^{0,n}\right)^2}{M(N-1)T} - 1, \tag{1.127}$$

as a measure of the degree of equipartition. We took a rod with length $L = 128d$, where d is the diameter, and persistence lengths $l_p = 10L$ (stiff), L (semi-flexible), $0.1L$ (flexible). The friction coefficients for a long cylinder, taken from Refs. [1, 2], were scaled by a dimensionless kinematic viscosity $\bar{\nu} = \nu/c_l d$. Here we consider typical values for actin filaments in water, $\bar{\nu} \sim 0.2$, and microtubules, $\bar{\nu} \sim 0.04$. Results are reported in Table 1.1.

The results in Table 1.1 show that the high frequency modes are in general well equilibrated; the energy in the shear and extensional modes is close to

			DEOM				DH			
$\bar{\nu}$	N	L/l_p	$\lvert\alpha_{1,2}\rvert$	$\lvert\alpha_3\rvert$	$\lvert\beta_{1,2}\rvert$	$\lvert\beta_3\rvert$	$\lvert\alpha_{1,2}\rvert$	$\lvert\alpha_3\rvert$	$\lvert\beta_{1,2}\rvert$	$\lvert\beta_3\rvert$
0.04	32	0.1	0.00	0.01	0.11	0.01	0.01	0.01	0.11	0.01
0.04	32	1.0	0.04	0.01	0.14	0.09	0.00	0.02	0.12	0.02
0.04	32	10	0.39	0.13	0.26	0.47	0.00	0.02	0.20	0.16
0.04	128	0.1	0.00	0.00	0.01	0.01	0.0 0	0.0	0.01	0.01
0.04	128	1.0	0.00	0.01	0.02	0.01	0.00	0.01	0.02	0.01
0.04	128	10	0.03	0.17	0.05	0.04	0.00	0.00	0.06	0.01
0.04	512	0.1	0.00	0.00	0.10	0.00	0.00	0.00	0.01	0.00
0.04	512	1.0	0.00	0.03	0.01	0.01	0.00	0.00	0.00	0.01
0.04	512	10	0.01	0.12	0.01	0.00	0.00	0.00	0.01	0.00
0.2	32	0.1	0.00	0.03	0.08	0.01	0.00	0.03	0.07	0.00
0.2	32	1.0	0.01	0.02	0.13	0.12	0.01	0.02	0.12	0.02
0.2	32	10	0.09	0.03	0.38	0.57	0.00	0.01	0.39	0.16
0.2	128	0.1	0.00	0.00	0.04	0.02	0.00	0.00	0.04	0.02
0.2	128	1.0	0.00	0.00	0.02	0.02	0.00	0.00	0.02	0.02
0.2	128	10	0.00	0.03	0.07	0.06	0.00	0.00	0.06	0.02
0.2	512	0.1	0.00	0.00	0.01	0.00	0.00	0.00	0.01	0.00
0.2	512	1.0	0.00	0.00	0.01	0.00	0.00	0.00	0.01	0.00
0.2	512	10	0.00	0.03	0.02	0.00	0.00	0.00	0.01	0.00

Table 1.1. Equipartition in simulations of an elastic rod with forces derived from discretized of motion (DEOM), Eqs. (1.121)–(1.122), and a discretized Hamiltonian (DH), Eqs. (1.123)–(1.124). The coefficients α_i and β_i, Eqs. (1.126)–(1.127) are shown in each case; the coefficients in the 1 and 2 directions are the same on average by symmetry. The results are fully converged with respect to time step; making Δt smaller does not materially change the result.

equipartition, $|\alpha_i| \approx 0$, in most cases. However, with a coarse spatial resolution ($N = 32$), there can be significant deviations from equipartition when the conservative forces are not exactly Hamiltonian. With a finer resolution the discretized continuum equations approach the Hamiltonian limit and equipartition is satisfied. When the viscous damping is small, the Hamiltonian forces lead to better thermal equilibrium in the filament, but when the damping is large the differences are small.

The bending modes are much softer and more prone to deviations from equipartition. For flexible filaments ($L/l_p = 10$), the displacements are large and the Hamiltonian is no longer quadratic in the curvature unless the number of segments is large. In the highly overdamped case, $\bar{\nu} \sim 0.2$, up to 500 segments are needed for good equipartition.

1.19 Summary

The theme of these lectures has been that an underlying Hamiltonian structure offers opportunities for more accurate and efficient solutions than is possible with generic numerical methods. In general my personal preference is for

simple methods, because it is not uncommon that sophisticated algorithms are disappointing when applied to complex problems. For example, implicit integrators work very nicely for individual elastic filaments, but can be quite inefficient when there are excluded-volume interactions. Most numerical methods are therefore an intricate tradeoff of advantages and disadvantages. But symplectic methods seem to have few if any disadvantages; they are straightforward to implement, more stable and more accurate than the standard ODE solvers.

Operator splitting is a flexible and powerful framework for developing new integration algorithms. Although there has been a lot of work on applications to Hamiltonian dynamics of interacting particles, I believe there is scope for further research, particularly for continuum systems and systems with thermal fluctuations.

Acknowledgments

This work was supported in part by the Alexander von Humboldt Foundation.

References

1. Cox, R.G.: The motion of long slender bodies in a viscous fluid.part l. general theory. J. Fluid Mech. **44**, 791–810 (1970)
2. Cox, R.G.: The motion of long slender bodies in a viscous fluid.part 2. shear flow. J. Fluid Mech. **45**, 625–657 (1971)
3. Dichmann, D.J., Maddocks, J.H.: An impetus-striction simulation of the dynamics of an elastica. J. Nonlinear Sci **6**(3), 271–292 (1996)
4. Dullweber, A., Leimkuhler, B., McLachlan, R.: Symplectic splitting methods for rigid body molecular dynamics. J. Chem. Phys. **107**(15), 5840–5851 (1997)
5. Dünweg, B., Ladd, A.J.C.: Lattice-Boltzmann simulations of soft-matter systems. Adv. Polym. Sci. **221**, 89–166 (2009). DOI 10.1007/978-3-540-87706-6
6. Ermak, D.L., McCammon, J.A.: Brownian dynamics with hydrodynamic interactions. J. Chem. Phys. **69**, 1352 (1978)
7. Everaers, R., Julicher, F., Ajdari, A., Maggs, A.C.: Dynamic fluctuations of semiflexible filaments. Phys. Rev. Lett. **82**(18), 3717–3720 (1999)
8. Fabritiis, G.D., Serrano, M., Español, P., Coveney, P.: Efficient numerical integrators for stochastic models. Physica A **361**, 429–440 (2006). DOI 10.1016/j.matcom.2006.05.019
9. Fixman, M.: Simulation of polymer dynamics. 1. General theory. J. Chem. Phys. **69**(4), 1527–1537 (1978)
10. Forbert, H.A., Chin, S.A.: Fourth-order algorithms for solving the multivariable langevin equation and the kramers equation. Phys. Rev. E **63**(1), 016,703 (2000). DOI 10.1103/PhysRevE.63.016703
11. Forest, E., Ruth, R.D.: Fourth-order symplectic integration. Physica D **43**(1), 105 – 117 (1990). DOI 10.1016/0167-2789(90)90019-L

12. Gans, J., Shalloway, D.: Shadow mass and the relationship between velocity and momentum in symplectic numerical integration. Phys. Rev. E **61**(4), 4587–4592 (2000). DOI 10.1103/PhysRevE.61.4587
13. Gompper, G., Ihle, T., Kroll, D.M., Winkler, R.G.: Multi-particle Collision Dynamics: A Particle-Based Mesoscale Simulation Approach to the Hydrodynamics of Complex fluids. Advan. Polym. Sci. **221**, 1–87 (2009). DOI 10.1007/978-3-540-87706-6
14. Kloeden, P.E., Platen, E.: Numerical solution of stochastic differential equations. In: Applications of Mathematics 23. Springer (1993)
15. Ladd, A.J.C., Kekre, R., Butler, J.E.: A comparison of the static and dynamic properties of a semi-flexible polymer using lattice-boltzmann and brownian dynamics simulations. Phys. Rev. E (2009). URL arXiv:0905.2434. Submitted
16. Ladd, A.J.C., Misra, G.: A symplectic integration method for elastic filaments. J. Chem. Phys. **130**(12), 124909 (2009). DOI 10.1063/1.3077863
17. Llopis, I., Pagonabarraga, I., Lagomarsino, M.C., Lowe, C.P.: Sedimentation of pairs of hydrodynamically interacting semiflexible filaments. Phys. Rev. E **76**(6, Part 1), 061,901 (2007). DOI 10.1103/PhysRevE.76.061901
18. Miller, T.F., Eleftheriou, M., Pattnaik, P., Ndirango, A., Newns, D., Martyna, G.J.: Symplectic quaternion scheme for biophysical molecular dynamics. J. Chem. Phys. **116**(20), 8649–8659 (2002). DOI 10.1063/1.1473654
19. Milstein, G.N., Tretyakov, M.V.: Quasi-symplectic methods for Langevin-type equations. IMA J. Numerical Analysis **23**(4), 593–626 (2003)
20. Milstein, G.N., Tretyakov, M.V.: Computing ergondic limits for Langevin equations. Physica D **229**(4), 81–95 (2007)
21. Öttinger, H.C.: Stochastic Processes in Polymeric Fluids. Springer-Verlag (1996)
22. Sanz-Serna, J.M.: Runge-Kutta schemes for hamiltonian systems. BIT Numer. Math. **28**, 877–883 (1988). DOI 10.1007/BF01954907
23. Serrano, M., Fabritiis, G.D., Español, P., Coveney, P.: A stochastic trotter integration scheme for dissipative particle dynamics. Math. Comput. Simul. **72**, 190–194 (2006). DOI doi:10.1016/j.matcom.2006.05.019
24. Suzuki, M.: General theory of fractal path integrals with applications to many-body theories and statistical physics. J. Math. Phys. **32**(2), 400–407 (1991). DOI 10.1063/1.529425
25. Uhlenbeck, G.E., Ornstein, L.S.: On the theory of the Brownian motion. Phys. Rev. **36**(5), 823–841 (1930). DOI 10.1103/PhysRev.36.823
26. Wada, H., Netz, R.R.: Non-equilibrium hydrodynamics of a rotating filament. Europhys. Lett. **75**(4), 645–651 (2006). DOI 10.1209/epl/i2006-10155-0
27. Zhong, G., Marsden, J.E.: Lie-poisson hamilton-jacobi theory and lie-poisson integrators. Phys. Lett. A **133**(3), 134–139 (1988)
28. van Zon, R., Omelyan, I.P., Schofield, J.: Efficient algorithms for rigid body integration using optimized splitting methods and exact free rotational motion. J. Chem. Phys. **128**(13), 136102 (2008). DOI 10.1063/1.2889937